Deep–Sea Research I 178 (2021) 103644

Contents lists available at ScienceDirect

Deep-Sea Research Part I

journal homepage: www.elsevier.com/locate/dsri

Revised depth of the Challenger Deep from submersible transects; including a general method for precise, pressure-derived depths in the ocean

Samuel F. Greenaway [a,*], Kathryn D. Sullivan [b], S. Harper Umfress [c], Alice B. Beittel [a], Karl D. Wagner [a]

[a] National Oceanic and Atmospheric Administration, Office of Marine and Aviation Operations, 8403 Colesville Road, Silver Spring, MD, 20910, USA
[b] Potomac Institute, 901 N. Stuart St., Suite 1200, Arlington, VA, 22203, USA
[c] National Oceanic and Atmospheric Administration, Office of Coast Survey, 7600 Sand Point Way, Seattle, WA, 98115, USA

ARTICLE INFO

Keywords:
Ocean pressure
Pressure to depth
Ocean gravity
Challenger Deep
Mariana Trench

ABSTRACT

We present a revised estimate of the maximum depth of the Challenger Deep, generally considered the deepest area of the world's oceans, based on a series of submersible dives conducted in June 2020. These depth estimates are derived from acoustic altimeter profiles referenced to in-situ pressure and corrected for observed oceanographic properties of the water-column, atmospheric pressure, gravity and gravity-gradient anomalies, and water-level effects. We also present comprehensive methods to determine depth from observed pressure using modern standards and estimate the associated uncertainty. For the Challenger Deep, the deepest observed seafloor depth was 10,935 m (±6 m at 95% C.I.) below mean sea level. For this work, the error term is dominated by the uncertainty of the pressure sensor used but we show that the gravity correction is substantial. We compare to these new results other recent acoustic and pressure-based measurements for the Challenger Deep.

1. Introduction

In June of 2020 Victor Vescovo conducted multiple dives to the bottom of the Challenger Deep, the deepest point in the Marianas Trench and deepest known area of the world's oceans. Using the crewed deep submergence vehicle (DSV), *Limiting Factor*, and three instrumented landers, Vescovo and his team made six successful transects across areas of the Challenger Deep identified from ship-based mapping efforts as candidates for the deepest location. Based on the short-range altimeter records vertically referenced using hydrostatic pressure, the deepest observed seafloor depth was 10,935 m (±6 m at 95% C.I.) below mean sea level. In calculating this depth, we develop here a rigorous approach to deriving pressure-based depth measurements using the modern oceanographic standards (IOC, SCOR and IAPSO, 2010) and present an associated error model. We compare our results with modern estimates from both surface-based mapping campaigns and direct pressure-based measurements. Apart from the obvious interest in refining the depth estimate of the deepest part of the ocean, we hope that the methods outlined here help with other high-precision, pressure-based measurements in the ocean. To date, the inaccuracy of available pressure sensors has precluded such precise work against a stable datum like mean-sea level. Ongoing advances in instrumentation have now opened this avenue, and we hope that the detailed analysis and methods shown here will be useful in other applications. Accordingly, we detail both the theory and methods of determining depth from observed pressure as well as validating the accuracy of a pressure sensor deployed to the bottom of the ocean.

Anyone who has swum even a few meters below the surface has experienced how hydrostatic pressure increases with depth, and pressure has long been a key part of the study of the oceans. Early oceanographic practice was built around the assumption that highly accurate direct pressure or height measurements were not practicable, so other proxies – such as derived geostrophic heights – have long been the tools used by oceanographers (Puig, 2018). In the oceanographic community, measured properties of the water column are used to infer baroclinic currents as well as turbulence and mixing (e.g., Taira et al., 2005; van Haren et al., 2017 for examples in the Challenger Deep). In the mapping and charting community, submerged pressure gauges are used to monitor water levels and, before the introduction of modern mapping systems, diver-held pressure gauges were a widespread tool for

* Corresponding author.
E-mail addresses: samuel.greenaway@noaa.gov (S.F. Greenaway), samuel.umfress@noaa.gov (S.H. Umfress), alice.beittel@noaa.gov (A.B. Beittel), karl.wagner@noaa.gov (K.D. Wagner).

https://doi.org/10.1016/j.dsr.2021.103644
Received 17 June 2021; Received in revised form 12 October 2021; Accepted 17 October 2021
Available online 21 October 2021

measuring depths on submerged hazards (Umbach, 1976). As the accuracy of pressure gauges and corresponding mapping requirements have increased, these studies have developed beyond the early basin-wide correction tables (e.g., Bialek, 1966). The increased use of autonomous underwater vehicles for mapping applications has required attention to the vertical position of the vehicle within the water column (e.g., Jalving, 1999; Willumsen et al., 2007). Engineering structures on the deep seabed require precise positioning and metrology (Puig, 2018). Despite advances in pressure gauges, pressure sensor calibration and drift remain a challenge (Polster et al., 2009). Recent work has featured innovative approaches to removing this drift with in-situ calibration routines (Sasagawa et al., 2016). Where pressure-based measurement applications in the ocean demand high precision, many current workers use a relative rather than an absolute datum. Some examples of these relative datum-type approaches that obtain *relative* precision on the order of cm to mm are: high-pass filtering in time for tsunami monitoring (Eble and Gonzalez, 1991); using a campaign of measurements of seafloor benchmarks to infer movement of a submerged volcano relative to the stable seafloor around it (Chadwick et al., 2006); and comparison of relative bottom-pressures across an ocean basin to infer mass-transport in the oceans (Fujimoto et al., 2003). In each of these cases, the high reported precision is only relative to other measurements nearby in time or space and not to a reference datum like mean sea-level.

In other applications, measurement of sea-surface heights with modern satellite altimetry data, coupled with high-accuracy bottom pressure measurements show promise to better understand oceanographic circulation and help tease apart the drivers of sea-level rise between volumetric (i.e. more total water in the oceans) and steric effects (i.e. expansion of the oceans due to increased heat content) (see Williams et al., 2015 for an experimental example and Vinogradova et al., 2007 for a model-based analysis). What is missing from the literature, to date, is a comprehensive method for accurately determining the depth from pressure relative to an absolute datum, such as mean sea level, at the precision that is now supportable with modern pressure sensors. We provide that here.

1.1. The general features of the Challenger Deep and the locations of depth estimates

The deepest section of the Marianas Trench, the Challenger Deep, is located approximately 200 nm SW of Guam. With a broad analysis of existing data, Stewart and Jamieson (2019) reinforced the general consensus that the Challenger Deep is the deepest location in the world's oceans. This was further bolstered by the results of the mapping component of the Five Deeps Expedition (Bongiovanni et al., 2021), which sought to locate and map the deepest locations in each of the world's oceans. Since the efforts of the HMS *Challenger* in 1952 (Carruthers and Lawford, 1952) and the R/V *Stranger* in 1959 (Fisher, 2009), the Challenger Deep has been recognized to consist of an elongated section with distinct subbasins or sediment-filled pools. As detailed by Nakanishi and Hashimoto (2011) the Challenger Deep consists of three depressions or basins along the axis of the trench, referred to as the eastern, central, and western basins. There is little agreement as to which basin is deepest or the deepest overall depth. The maximum depth estimates discussed in this report are located in and around each basin (Table 1, Fig. 1).

1.2. A brief history of depth measurements of the Challenger Deep

Others have recently given comprehensive accounts of the history of the depth measurements in the Challenger Deep, starting with the famous world-circling expedition of the HMS *Challenger* in 1873–76 (e.g., Nakanishi and Hashimoto, 2011; Gardner et al., 2014). While interesting from a historical perspective, the accuracy of methods such as taut-wire sounding (e.g., Carruthers and Lawford, 1952) or hand-tossed explosives and aurally detected returns (e.g., Fisher, 1953) have been surpassed by modern methods with respect to accuracy, coverage, and resolution and we do not include those measurements in our comparisons.

1.2.1. Modern acoustic measurements

Since the adoption of modern multibeam echosounders, a number of missions have mapped the Marianas Trench in the vicinity of the Challenger Deep. Neither the locations nor values of the reported maximum depths are in agreement between many of these missions. Most recently: Taira et al. (2005) used a full profile conductivity, temperature and depth (CTD) casts from 1992 to correct the contemporaneous (1992) readout depth of a SEA-BEAM 500 operated as a single beam and reported a maximum depth of 10,989 m with no uncertainty reported; Nakanishi and Hashimoto (2011) used data from a number of Japanese cruises around the early 2000's and calculated a maximum depth of 10,920 ± 5m (at 95% C.I.) in the eastern basin; Gardner et al. (2014) determined a maximum depth of 10,984 ± 25 m (at 95% C.I.) in the western basin based on data acquired in 2010 from a EM122 on the USNS *Sumner*; van Haren et al. (2017) reported a depth of 10,925 ± 12 m (at 95% C.I.) in the western basin using the 2016 data from the EM122 on the R/V *Sonne*; Bongiovanni et al. (2021) reported a maximum depth in the eastern basin of 10,924 ± 15 m (at 95% C.I.) from a EM124 during the Five Deeps Expedition; Loranger et al. (2021) opportunistically used the impulse from an imploding instrument and reported a depth of 10,983 ± 6 m (reported at 1-sigma, roughly 12 m at 95% C.I.) near the central basin.

The disagreement between these maximum depth estimates exceeds the estimated uncertainty of each, a situation which calls into question either the measurement or the reported uncertainty. Additionally, the location of reported deepest locations differs substantially between reports. Since the advent of global satellite positioning systems used for positioning of these modern mapping missions from the 1990's onward, the horizontal accuracy of the ship position is likely on order of meters to tens of meters. However, the effective horizontal resolution from the

Table 1
Published depths discussed in this paper. Year is when the measurement was made. Letter corresponds to location on Fig. 1.

Letter	Platform	Year	Lat	Long	Depth (m)	Source
A	R/V Vityaz	1957	11°20.9′N	142°11.5′E	11,034	Taira et al. (2005) citing Hansen, 1959
B	Trieste	1960	11°18.5′N	142°15.5′E	10910	Piccard and Dietz (1961)
C	R/V Hakuho Maru	1992	11°22.6′N	142°35.0′E	10,989	Taira et al. (2005)
D	ROV Kaiko	1997	11°22.1′N	142°35.4′E	10,911	Takagawa et al. (1997)
E	R/V Kairei	2002	11°22.3′N	142°35.6′E	10,920	Nakanishi and Hashimoto (2011)
F	ROV Nereus	2009	11°22.1′N	142°34.4′E	10,903	Fletcher et al. (2009)
G	USNS Sumner	2010	11°19.8′N	142°12.0′E	10,984	Gardner et al. (2014)
H	DSV Deepsea Challenger	2012	11°22.2′N	142°35.4′E	10,908	Gallo et al. (2015)
I	Deepsea Challenger Lander	2012	11°22.1′N	142°26.0′E	10,918	Gallo et al. (2015)
J	Mk III Implosion	2014	11°21.3′N	142°27.2′E	10,983	Loranger et al. (2021)
K	USCGC Sequioia	2015	11°20.1′N	142°12.0′E	10,854	Dziack et al. (2017)
L	R/V Sonne	2016	11°19.9′N	142°12.1′E	10,925	van Haren et al. (2017)
M	DSV Limiting Factor	2020	11°22.3′N	142°35.3′E	10,935	this paper

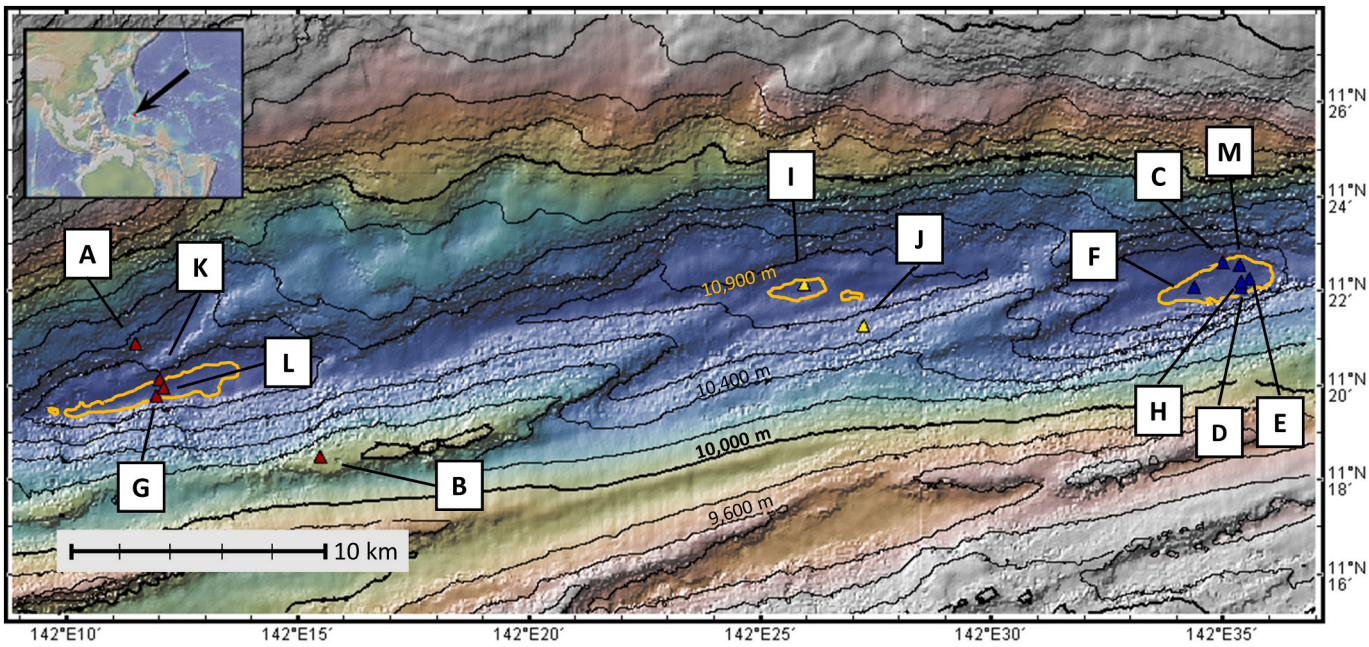

Fig. 1. The Challenger Deep consists of three basins over 10,900 m deep. 10,900 m contour shown in orange. Maximum depth estimates discussed in this report are shown by red triangles in the western basin, yellow triangles in the central basin, and blue triangles in the eastern basin. Labels reference Table 1. Bathymetry from Bongiovanni et al. (2021).

surface-ship mapping systems (and thus the overall precision of the position of the depth estimate) is on order of hundreds of meters (Gardner et al., 2014; Nakanishi and Hashimoto, 2011). The individual basins, however, are separated by tens of km.

Van Haren et al. (2017) and Loranger et al. (2021) argue that the difference between the various acoustic depth results may be due to different strategies used to determine the sound speed profile through the water column, a critical aspect of any acoustic ranging measurement (Beaudoin et al., 2009). We compare these profiles and examine the impact of the different sound speed equations used by these authors in section 5.1, finding that the sound speed alone is insufficient to explain the differences.

1.2.2. *Pressure-based measurements*

Prior to the *Limiting Factor*, only two crewed submersibles, three uncrewed vehicles, and a small number of free-fall landers are known to have visited the Challenger Deep: Jacques Piccard and Don Walsh in *Trieste* in 1960, the Japanese Agency for Marine-Earth Science and Technology's (JAMSTEC) remotely operated vehicle (ROV) *Kaiko* in 1995 and 1998, JAMSTEC's ROV *ABISMO* in 2008, the Woods Hole Oceanographic Institution's hybrid autonomous/remotely-operated underwater vehicle *Nereus* in 2009, and James Cameron in *Deepsea Challenger* in 2012.

Trieste observed a pressure-derived depth of 10,910 m (Piccard and Dietz, 1961). No uncertainty was reported with this depth and we have been unsuccessful in locating the original pressure instrument in the U.S. Navy's historical artifact collections to better estimate the associated uncertainty. Piccard reported that the pressure gauge was originally calibrated in fresh water, and corrections for salinity, temperature, temperature, and gravity were later applied by J. Knauss of Scripps Institute of Oceanography and Dr. J. Lyman of the National Science Foundation. Fisher (2009) reported that Art Maxwell from the Office of Naval Research issued a notice on March 10, 1961 correcting the *Trieste* depth to 10,913 ± 5 m. However, we have been unable to identify the details of these corrections or find an analysis of the uncertainty in the literature. *Kaiko* reportedly reached a maximum depth of 10,911 m in 1996 (Takagawa et al., 1997) and 10,924 m in 1998 (Barry and Hashimoto, 2009). While Takagawa et al. state that the observed pressure was corrected for temperature and salinity, the details of the calculations and associated uncertainty were not published. The ROV *ABISMO* reached 10,257 m, but Yoshida et al. (2009) acknowledged that the deepest part of the trench was not visited because of limited cable length. *Nereus* reportedly reached 10,903 m (Fletcher et al., 2009), but details of the calculation and uncertainties were not published. *Deepsea Challenger* dove to a depth of 10,908 ± 3 m and un-crewed landers deployed with that mission observed depths of 10,918 ± 3 m (Gallo et al., 2015). Additionally, Dziak et al. (2017) deployed a bottom-moored hydrophone and pressure sensor in 2015 and calculated a bottom depth of 10,854 m. However, they noted that the position of the dropped sensor was likely not in the deepest possible location.

2. Materials and methods

2.1. *Instrument configuration, general strategy, and software*

Prior to conducting submersible dives, the vicinity of the trench was mapped using the ship-mounted EM124 multibeam of the support ship *Pressure Drop* (Bongiovanni et al., 2021). This map was then used to plan the submersible dives across the deepest parts of each basin. The instrumentation suite for the *Limiting Factor* dives consisted of up to three instrumented free-fall landers and instrumentation on the submersible itself. Each lander was fitted with a pressure gauge (RBRsolo3D|Deep) and CTD sensor (Seabird SBE49). The submersible had an acoustic altimeter (Kongsberg 1107) and three CTD sensors (Seabird SBE49). The landers were deployed before the submersible and remained on the seabed during the dive. The landers were used for navigation on the seabed, and each dive rendezvoused with at least one lander on the seabed.

The RBR pressure gauges on the landers are twice as accurate as the pressure gauges in the CTD sensors (specified by the manufacturer at 0.1% of full scale or 10 m at 95% CI for the RBR vs 0.2% of full scale or 20 m at 95% CI for the CTD). In operation, we also observed drift at depth to be smaller with the RBR instruments than the pressure sensors in the CTD. The stable location of the sensors on the landers also allows us to model instrument drifts and verify correct application of water-level corrections.

Our general approach to estimate seafloor depth is to use the landers to establish a stable datum at the seafloor relative to mean-sea level (MSL). We then tie into this seafloor datum by passing by the lander location with the submersible-based altimeter. The submersible altimeter is vertically controlled by the on-board CTD pressure sensor, but the offset of this relatively inaccurate sensor is removed by the seafloor tie point with the lander-established datum. We use the Thermodynamic Equation of State of Seawater 2010) (TEOS-10; IOC, SCOR and IAPSO, 2010) and the associated Gibbs Seawater (GSW) toolbox (McDougal and Barker, 2011) to calculate the density of the water column and determine an initial depth estimate. In establishing a stable datum at the seafloor, we correct for: the in-situ observed density of the seawater from contemporaneous salinity and temperature profiles; surface gravity and gravity-gradient anomalies, water-levels (i.e., tides), and atmospheric pressure at the dive location. These corrections are discussed in section 3 where we detail our approach and develop an uncertainty estimate for each.

We used the open-source Python packages NumPy (Harris et al., 2020) and SciPy (Virtanen et al., 2020)) for data processing and analysis, Matplotlib (Hunter, 2007) for plotting figures, and GeoMapApp (http://www.geomapapp.org) for geographic figures.

2.2. Pressure sensor calibration and drift corrections

2.2.1. RBR pressure sensor drift and observed precision of lander depths

Before deployment, the RBR pressure gauges were calibrated against Paroscientific Inc., DigiQuartz pressure gauges independently at two facilities. The calibrations suggested accuracies considerably higher than specified for these instruments. The maximum difference between the three sensors and the reference standards was 0.6 dbar, roughly an order of magnitude smaller than the specified accuracy of the RBR gauges (0.1% of full scale or 10 m at 95% CI).

Following correction for density, gravity, water levels, and atmospheric pressure (as detailed in Section 3), the pressure records for the time the landers were on the seabed showed consistent drift characteristics across instruments and deployments. In all cases the pressure record drifted towards less pressure with time (as if the instrument were rising up in the water column). It is thus unlikely that the pressure change reflects a settling of the instrument into the seabed. This deep-to-shallow drift was also observed in the long-term deployment of a similar sensor in 2015 by Dziak et al. (2017) that we used to extract water levels (section 3.4.1). We extracted the seabed portion of the lander pressure records and fit a piecewise linear model (Fig. 2).

The initial drift of these gauges was 15±3 cm/h and the final drift 7±3 cm/h. On average, the inflection point was 4 h after the lander touched down, however, there was considerable variation in the time of this inflection point. We do not know the root cause of the drift or the differences in timing; drivers might include different descent rates or different thermal coupling to the environment. We subtracted the individually-fitted drift of the sensors on the seabed and then averaged the de-trended depth over the time on the seabed to obtain the estimate of the MSL relative depth at the lander location. We then used this depth to tie the submersible mounted instruments to the MSL datum when the submersible rendezvoused with the lander.

2.2.2. RBR pressure sensor accuracy and CTD pressure sensor drift from ganged sensor deployment

In three cases, two or three of the RBR pressure gauges were installed on a common platform. This allowed us to evaluate the relative accuracy of the sensors in practice. On June 20, all three RBR gauges were mounted at the same height on a single lander. On June 22, two RBR gauges were installed on one lander, and on June 26, all three RBR gauges were installed on the submersible. Using RBR Sn204134 as a reference, Sn204133 was consistently shallower by 4 m and Sn204135 was shallower by 1.5 m. We set RBR Sn204134 as the standard because it was deployed on the lander used for all submersible-lander rendezvous.

For the June 26 dive only, all three RBR sensors were installed on the submersible along with the CTDs. We used this dive to evaluate the drift of the submersible CTD pressure sensors. Fig. 3 shows the depth of the CTD sensor relative to RBR Sn204134. The apparent drift in this figure is two-fold; it includes both the drift of the RBR sensor and the CTD pressure sensor. The relative drift is approximately 0.5 m/h. We previously observed a deep-to-shallow drift of the RBR gauges when deployed on static landers. The CTD pressure sensor drifted from shallow to deep. We are confident in the magnitude and direction of the RBR sensor drift from the lander deployments (not appreciably more than 15 cm/hour). However, because the timing of the shift in RBR drift rates was variable in the lander deployments, we do not have confidence in being able to estimate the RBR drift absent reference to a stable datum (the submersible was moving through the dive). Therefore, it is difficult to determine the CTD drift from the comparison with the RBR gauges and we have not attempted to further correct for the CTD sensor drift. This does mean that when we use the submersible-mounted CTD pressure to control the vehicle depth, there is a drift on either side of the lander tie.

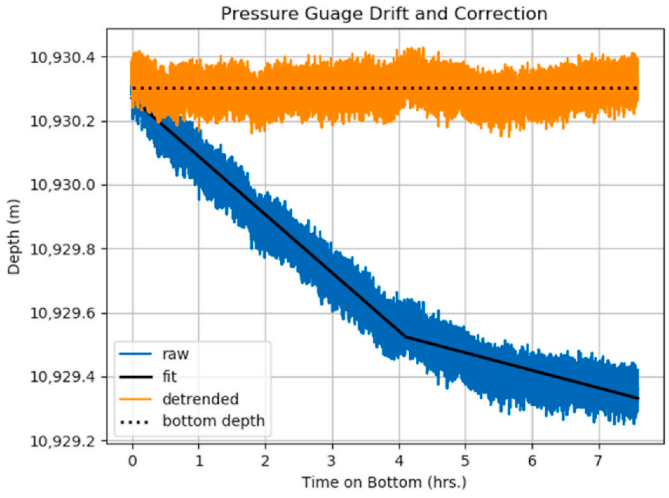

Fig. 2. Lander pressure drift during time on seafloor (this example from June 7 dive (Sn204134)). 'Raw' here is corrected for everything except sensor drift. Black line shows the two-part piecewise linear model which was used to remove the drift. Dotted line shows average depth of the de-trended gauge.

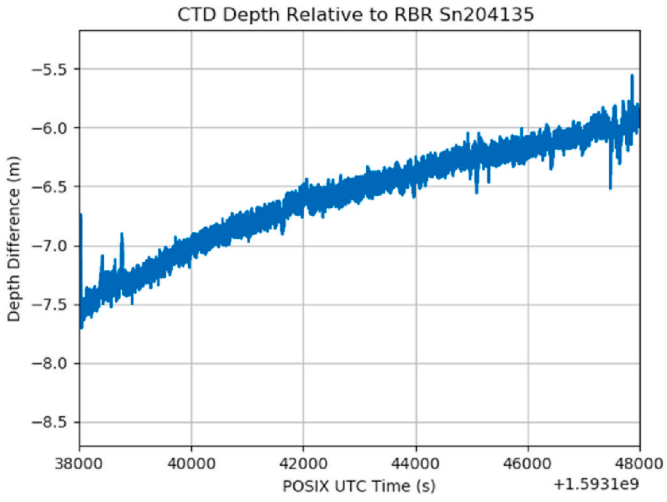

Fig. 3. Submersible-mounted CTD pressure-derived depth less the RBR Sn204134 derived depth for bottom segment of June 26 dive. Drift is a combination of RBR drift (from deep to shallow) and CTD pressure sensor drift (from shallow to deep).

The seafloor prior to the tie is biased progressively shallower away from the tie point. The seafloor after the lander tie point is biased progressively deeper. This drift is approximately 0.5 m/hour, though the CTD drift appears to be more exponential than linear, especially early in the deployment (Fig. 3). The CTD pressure sensor drift does not affect the depths at the lander tie points.

For the June 26 dive, because all three RBR gauges were mounted on the submersible we were unable to use the lander-tie approach to control the submersible depth. We used RBR Sn204134 to directly determine the vehicle depth. Because we did not have any measurement of the drift of this instrument when installed on the submersible, we have not corrected for RBR drift for this dive. However, based on the other deployments of this sensor, we are confident of the direction of the drift (from deep to shallow) and overall magnitude. This means that the reported depths of this dive are biased up to a meter shallow, with the points later in the dive biased more than those early in the dive.

2.3. Specific steps to calculate bottom depth from pressure and submersible altimeter records

1. Remove atmospheric pressure time series from pressure records
2. If pre-deployment surface pressures are available in record, remove to zero in-situ atmospheric pressure.
3. Using the conductivity, in-situ temperature, and pressure record from CTD profile, calculate Absolute Salinity (SA) and Conserved Temperature (CT) using GSW toolbox (gsw.SA_from_SP and gsw.CT_from_t).
4. Use the SA and CT profile to calculate dynamic height anomaly as a function of pressure (gsw.geo_strf_dyn_height).
5. Interpolate dynamic height anomaly to pressure at observed pressure
6. Calculate water column height (i.e. depth) using GSW toolbox (gsw.z_from_p) and interpolated dynamic height anomaly.
7. Correct for surface gravity anomaly and surface gravity gradient anomaly.
8. Apply water-level correctors to reduce observation to MSL datum
9. Apply vertical offsets from lander pressure sensor to seafloor
10. For landers, de-trend calculated depths and average to establish seafloor datum
11. Apply altimeter heights to submersible pressure from CTDs mounted on submersible to obtain uncorrected bottom depths.
12. At lander rendezvous points, tie altimeter observed seafloor to lander-established datum.

3. Theory and component uncertainty estimation

3.1. Pressure to depth calculations

From the hydrostatic equation of seawater, we use the equivalence of the pressure integral of the specific volume of the seawater and the vertical integration of the gravity. Both yield a potential known as dynamic height (IOC, SCOR and IAPSO, 2010). See Appendix A for a more comprehensive derivation and discussion of this equation.

$$\int_0^P a_0\, dp \;+\; \int_0^p \delta\, dp \;=\; \overline{g}H\,,\; \overline{g} = \frac{1}{H}\int_0^H g\, dh \tag{1}$$

Where a_0 is the specific volume of standard ocean, δ is the specific volume anomaly, g is gravity and H is the height of the water column. The integral of the specific volume anomaly, the second term of the left side of Eqn 1, contains the information on density from the CTD profile and is called the *dynamic height anomaly* or the *geopotential anomaly* (IOC, SCOR and IAPSO, 2010). Rearranging:

$$\frac{\int_0^P a_0 dp + \int_0^P \delta dp}{\overline{g}} = H \tag{2}$$

We note that the calculation of the average gravity over the water column necessarily involves knowing the height that forms the upper bound of the integral, thus Eqn 2 is not a strictly closed form. Substituting a linear pressure-to-depth approximation yields acceptably small error in most cases. This approximation is discussed in greater detail in section 3.3 Gravity in the Sea.

3.2. Estimation of CTD-Based uncertainty

We used a Monte Carlo method to estimate the depth uncertainty from the CTD measurement. We scaled a Gaussian random error to the specified accuracy of the Seabird sensor (conductivity: 0.0003 S/m, temperature: 0.002 °C, and pressure: 0.1% of full scale or 11 dbar), added a random error from those distributions to a measured profile (in this case a profile from June 26, 2020) and then calculated the depth from a pressure of 11,250 dbar (about 10,920 m). We repeated this process 1,000 times and calculated standard deviation of the resulting distribution of derived depths. To evaluate the sensitivity of the result to the three sensors in the CTD, we repeated this process for seven possible values of each instrument uncertainty centered on the reported uncertainty for a total of 343,000 trials. When the random error was freshly drawn for each point in the cast, the estimated depth uncertainty was 2 cm. When we applied the random error as a bias to all measurements in each modeled cast of our statistical ensemble, the estimated depth uncertainty was 11 cm. While there is likely some stochastic noise between each measurement within a profile, it is unreasonable to expect that the overall uncertainty should decrease with the number of measurements in a CTD profile, as it does when we apply the error on a point-by-point basis. Accordingly, we think the second method better captures the expected uncertainty from this CTD sensor when applied to this measurement. Over the range of values considered, we found the resultant uncertainty is linearly sensitive to changes in the pressure sensor accuracy, but not sensitive to changes in the temperature or conductivity sensor accuracy.

Williams et al. (2015) present a similar analysis of the expected pressure uncertainty from CTD uncertainty for the case of a tall-mooring with five of the same model CTD sensors distributed along the mooring. They report expected pressure variability from CTD uncertainty to be much lower (1 cm if correlated, 0.25 cm if uncorrelated). We think two factors explain the difference. Williams et al. (2015) assumed stated instrument accuracies are at two-sigma while we have used one-sigma (Seabird, personal communication, 2020). Additionally, the depth of our analysis is more than twice as deep (11 km vs 5 km). This second factor has two impacts. The first is that the sum of the errors is naturally larger over a larger column. The second is that the stated uncertainty of the pressure sensor is referenced to the full scale. We have used 11 km sensors in our analysis while we assume Williams et al. used sensors with maximum pressure ranges of less than 2.5 km. Overall, these factors account for a factor of up to 16 between our estimates. Interestingly, Williams et al. (2015) find that the conductivity and temperature measurements are limiting in their application, where the pressure sensor of the CTD clearly dominates the uncertainty in our case. This is likely because the absolute accuracy of our sensor is much poorer because of the greater depth range.

Taira et al. (2005) and van Haren et al., 2021 detail additional correction to hadal CTD profiles to account for subtle pressure effects. These are important for the stability and turbulence parameters considered in those works, but are not significant for our analysis and we have not applied these corrections.

3.3. Gravity in the sea

The gravity term in Eqn 2 merits attention. We show that corrections driven by the gravity term are relatively large compared to the other correctors we consider. As described by Hackney and Featherstone (2003), there are substantial differences between the geophysical, prospecting, and the geodetic communities on even some basic definitions of gravity, vertical gravity gradients, and various applied corrections. See Appendix B for more detailed derivations and discussions on gravity in the sea.

Both the UNESCO and TEOS-10 formulations use the ellipsoid based GRS 80 gravity model (Moritz, 1980) for the surface gravity as a function of latitude and a linear model of the variation of gravity with depth in the ocean given by

$$g(d) \cong g_0[1+\gamma d] \tag{3}$$

where g_0 is the surface gravity from the ERS 80 gravity model, $\gamma = 2.26 \times 10^{-7}$ 1/m, and d is the depth below the surface. Appendix B contains derivations of the gravity gradient.

To evaluate Eqn 2, we prefer to express gravity as a function of pressure rather than depth. Following McDougal (2010) and using the linear approximation of 0.98 m/dbar (i.e., assuming a constant density of 1.035 kg/m^3 and g = 9.7963 m/s^2, both average values for the ocean), we can write:

$$g(\varnothing, d) = g_{GRS80}(\varnothing)[1+\gamma p] \tag{4}$$

where the g_{GRS80} is given in equation g2 and is γ is 2.22×10^{-7} 1/dbar.

Because the impact of the gravity gradient on the calculated depth is small (though not negligible), using a linear pressure to depth relationship in figuring the gravity results in a small residual error - an error in γ of one per cent yields a depth error of 14 cm over 11 km.

3.3.1. Gravity anomalies and estimation of topographic effects

The non-uniform mass distribution of the earth, including bathymetry or topography, causes local differences in gravity from the uniform GRS 80 model, which are referred to as gravity and gravity gradient anomalies. Sandwell et al. (2014) determined these anomalies over the world's oceans and the model is available as a base layer in GeoMapApp. At the Challenger Deep dive site, the surface gravity anomaly is −320.85 mGal (Sandwell et al., 2014). Even this relatively large gravity anomaly is only 0.033% of the GRS 80 gravity at this location. However, in nearly 11 km of water, this anomaly alone results in a change in the depth (by Eqn 2) of 3.6 m. Here, the gravity anomaly corrected depth is deeper; with less gravity it takes a taller column of water to result in the same pressure. The magnitude of this correction is nearly half of that from the steric effects of temperature and salinity and cannot be ignored in a precision depth calculation in the deep ocean.

However, it was not obvious to what extent these surface anomalies captured the effects of the topography and density variations in our study area or how to assign uncertainties to this correction. The gravity model incorporated in the TEOS-10 and UNESCO formulations assumes a homogenous and bottomless ocean with a surface gravity given by the GRS 80 model. Our first idea was to use the in-situ seawater density. We show this has a small effect. More significantly, at the base of the Challenger Deep, a submersible is nearly 7 km below the average depth of the ocean. In the sense of a model of the earth comprised of shells of constant density, the submersible is beneath more rock than water. Ideally, we would downward propagate the surface gravity using the bathymetry and a model of the density of the earth to constrain the solution. Such downward continuation problems are generally ill-conditioned (Sebera et al., 2015), and global-scale calulations are difficult (see Hirt et al., 2013 for an example of the terrestrial case). To better understand the possible impact of the trench on the gravity field, we constructed a few simple models of the Challenger Deep where we could solve the gravitational field analytically:

1. Missing slab: we assumed the GRS 80 model described an earth with a uniform 4 km deep ocean and calculated the gravitational effect of a missing 7 km thick slab of rock (of density 2,700 kg/m^3).
2. Cylinder: we modeled the Challenger Deep as vertical cylinder centered on the dive site with a radius of 30 km and depth of 7 km.
3. Bore-hole: we again started with the GRS 80 model, but assumed that we bored into rock at 4 km with a negligibly small bore-hole from a gravity perspective.

The missing slab and bore-hole models should provide boundaries of the actual topographical effect of the Challenger Deep and the cylinder model should provide a better, though still crude model. We calculated the gravity, the gravity gradient, and the resultant change in calculated pressure derived depth for each of these models over the depth of Challenger Deep and compared the solution to the simple approach of using the surface gravity and gravity gradient anomaly as constants over the full depth of the ocean. In each case the depths calculated using the modeled gravity are greater than if using GRS 80 and Eqn 4 for depth dependence (Fig. 4).

At the depths of the Challenger Deep, the difference between a pressure-derived depth corrected with the missing slab model and the borehole model is 1.9 m. On the assumption that the actual gravity is somewhere between these two extremes, this serves as a reasonable outer bound on the uncertainty of the gravity correction. Recognizing that the surface gravity anomaly and surface gradient anomalies contain information about the topographic correction, the difference between the actual gravity and gravity modeled using the surface gravity and gravity gradient anomalies is likely substantially less than 1.9 m. The difference in depth calculated using the cylinder model and the surface anomalies is 0.4 m at full depth. Assuming that the actual topographic effect is likely somewhere in the middle of the two boundary cases (missing slab and borehole), we estimate the depth uncertainty due to residual terrain corrections as ±0.5 m. Without measuring the gravity directly or doing far more sophisticated modeling of the terrain effect, it is not possible to better constrain this estimate. The difference in depth accounting for the gravity effect of the in-situ water density is 0.13 m. Because the uncertainty in the topographic gravity correction is much larger than the total magnitude of the in-situ water density correction, we did not account for the in-situ water density when correcting for gravity. We did use the surface gravity anomaly and surface gravity gradient anomaly to correct the average gravity over the column.

3.3.2. Correction of depth for surface gravity anomaly and gravity gradient anomaly

Given Eg. 2, we can correct a depth for a different gravity field by multiplying by the GRS 80 average gravity over the column and dividing by the corrected average gravity over the column. For a gravity model of form of Eqn 3, the average gravity over the column is:

$$\overline{g}(\varnothing, d) = g_{GRS80}(\varnothing)\left(1+\frac{\gamma H}{2}\right) \tag{5}$$

Correcting a depth, H, that had been calculated using the standard GRS 80 model to account for a gravity anomaly, A, and gravity gradient anomaly, B, is:

$$H_c = H\frac{g_{GRS80}(\varnothing)\left(1+\frac{\gamma H}{2}\right)}{g_c(\varnothing)\left(1+\frac{\gamma_c H}{2}\right)} \quad g_c(\varnothing) = g_{GRS80}(\varnothing) + A \quad \gamma_c = \gamma + \frac{B}{g_c} \tag{6}$$

Strictly speaking, the H in the denominator of the right-hand side of Eqn 6 should be H_c, but the effect of replacing it with H as shown here is negligible for physically reasonable values of the gravity and gravity gradient anomalies.

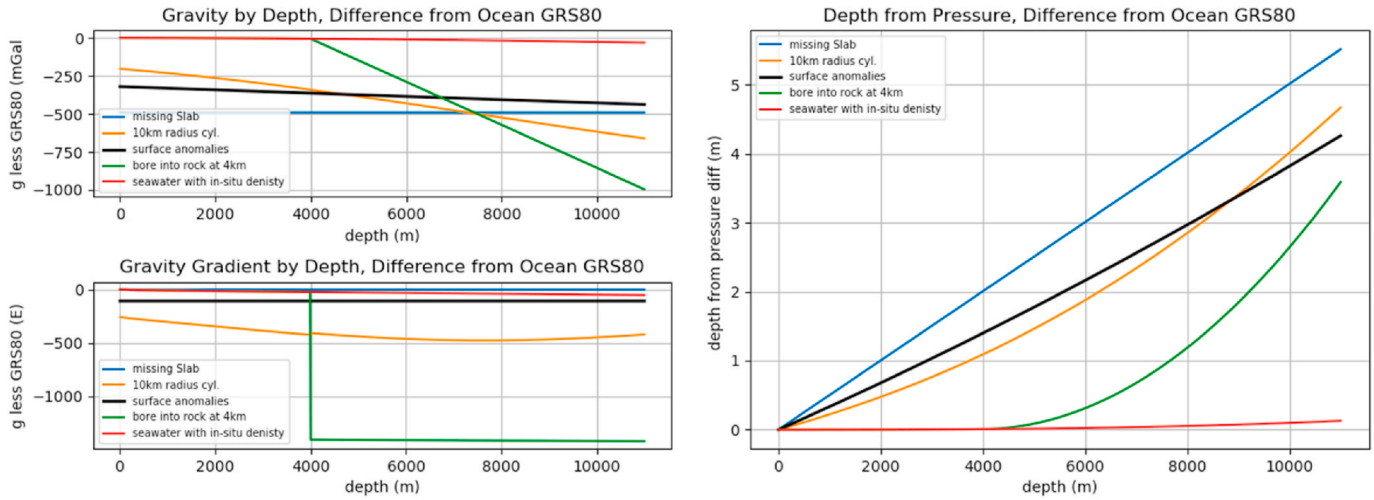

Fig. 4. Difference from GRS 80 of modeled gravity by depth (top left), gravity gradient (bottom left) and the resultant change in calculated depth from pressure (right) for the simple models (missing slab, cylinder, and borehole into rock) to correct for topography of the Challenger Deep. Surface gravity anomaly and surface gravity gradient anomaly used as constants is shown in heavy black line and gravity correction for the in-situ water density is shown in red.

3.4. Reduction to datum, atmospheric pressure and tides

So far, this analysis has focused on deriving an instantaneous depth from an observed pressure, i.e., how much water is over the top of a pressure sensor. For our work, we want to know depths relative to a stable datum such as mean sea level (MSL). For this we need to model or measure where the surface of the sea is relative to this datum and look at two drivers of the instantaneous sea level, atmospheric loading and tidally driven water-levels. We neglect wind driven surface waves or swell. By linear wave theory, the pressure variations of even very large surface waves would be indistinguishable at hadal depths.

3.4.1. Water-level correction

In the mapping community, *tides* refer to the harmonic aspects of the level of the ocean, while *water-levels* captures the tides plus any non-tidal changes to the water level such as from wind stress or atmospheric loading. We used a water-level approach and a non-harmonic comparison method (Parker, 2007) to correct the instantaneous water level at the time of the measurement to a stable datum. Here, we choose mean-sea level (MSL) as the reference datum. We used the nearly 60-day long deployment of a hydrophone and pressure sensor to the Challenger Deep by NOAA's Pacific Marine Environmental Laboratory in 2015 (Dziak et al., 2017) to determine a water-level model for the Challenger Deep referenced to the National Water Level Observation Network (NWLON) reference station at Apra Harbor in Guam. The water-level signal observed at Guam is similar in character to the variations seen in the 2015 Challenger Deep pressure records (Fig. 5) with the addition of substantial drift in the pressure record (~3 m over 50 days). Observing that there were not significant phase offsets between the water-level and pressure derived depths, we calculated a 6-min average for the pressure measurements (to match the water-level gauge), differenced the two to estimate drift, and then fit a model to this difference. We modeled this drift using the same equation used by Polster et al. (2009), acknowledging that the sensors addressed in that work, Paroscientific Digiquarz, are different from the strain gauges used here. This drift equation is:

$$P = Ae^{-Bt} + \mathrm{Ct} + \mathrm{D} \tag{7}$$

With fit values shown in Table 2.

The difference and the fit are shown in the right panel of Fig. 5. We also modeled the drift with a third order polynomial, but the performance of the exponential equation was clearly superior.

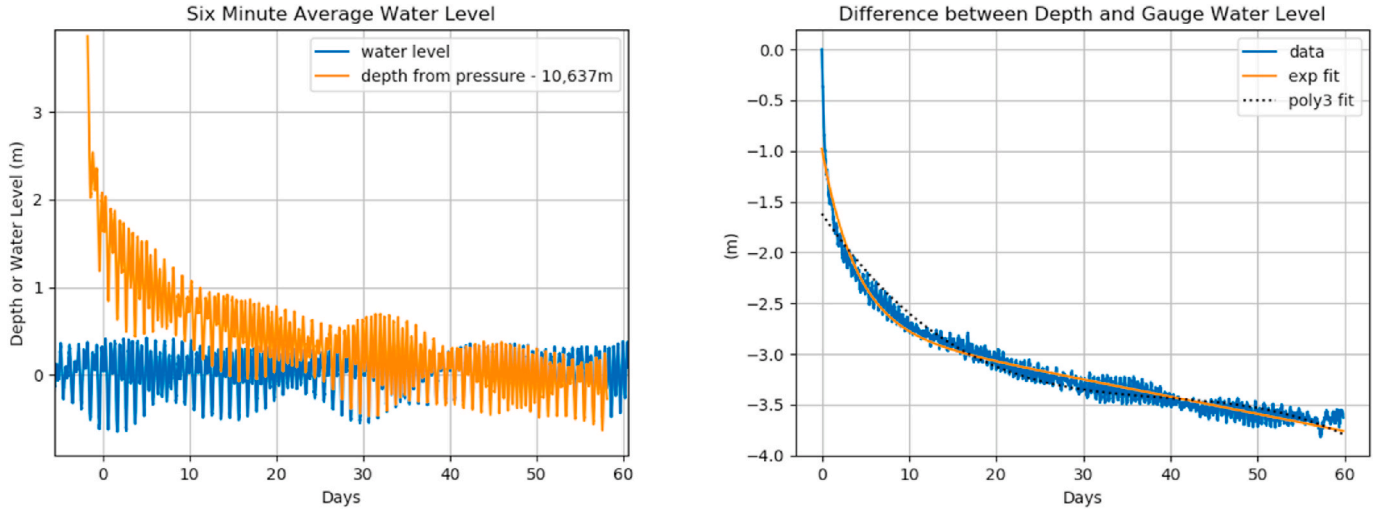

Fig. 5. Six-minute average data from pressure derived depth and water level gauge (left). Difference between pressure derived depth and water-level from gauge (right) with fitted distributions. The exponential based model of Eqn 7 (shown in solid orange) is used here.

Table 2
Pressure sensor drift parameters for 2015 deployment by Dziak et al. We used this deployment to determine water-level corrections for the Challenger Deep. Fit from Eqn 7.

Parameter	Value	Unit
A	1.760	m
B	0.255	1/day
C	−0.017	m/day
D	−2.740	m

After correcting for the modeled sensor drift, we calculated an amplitude correction of 120% and no phase offset between the Guam gauge and Challenger Deep using the Tide-by-Tide method (Parker, 2007). That is, compared to the reference gauge in Guam, the amplitude of the tide signal at the Challenger Deep has a 20% larger amplitude but occurs at same time. Following correction for drift and amplitude adjustment, there was an 8 cm (1-sigma) residual error in applying the Guam gauge data to the Challenger Deep for the 2015 pressure data (Fig. 6). One could use more sophisticated water-level models to increase the precision of the water-level term. However, for this work, the residual error in the water level term is small compared to other sources of error.

Using the established MSL datum at Guam to develop the water-level correctors at the Challenger Deeo gives us a model that includes any geoid undulations between the gauge and our site but that does not capture any variation in the topography of the sea-surface (i.e., the separation between MSL and the geoid) between the two locations. Future expeditions could use either a ship or a buoy to directly position the sea-surface relative to a datum such as the WGS84 ellipsoid using GNSS methods. In such a case, the datum offset between ellipsoid and MSL that accounts for both the geoid and topography of the sea surface at the site of the measurement is required. For this mission, we did not have high-precision vertical GNSS positions from the ship or a validated datum offset model.

We neglect solid earth tides in this analysis, implicitly assuming that tidal deformation of the earth at the reference station in Guam is the same as at the dive site. For very high precision and in cases where the sea surface is positioned by either a GNSS buoy or satellite altimetry, solid earth tides may need to be considered.

We subtracted the modeled water-levels at the dive site from all calculated depths to reference to the mean sea level datum. Because our water level model is based on a nearby reference station, the water levels include tidal factors as well as non-tidal factors such as wind stress and atmospheric loading.

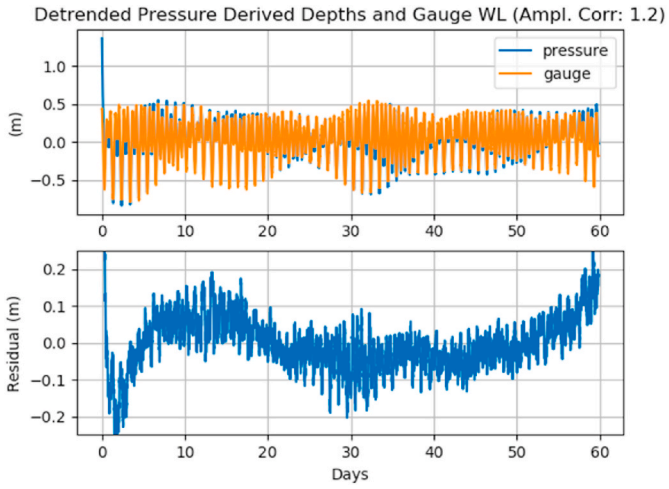

Fig. 6. Pressure derived depth of 2015 hydrophone deployment with modeled drift removed compared to Guam water levels with 1.20 amplitude correction. RMS of the residuals is 8 cm (1-sigma).

3.4.2. Atmospheric pressure

Increased atmospheric pressure tends to depress the local sea level in an effect known as the inverse barometer effect (Wunch and Stammer, 1997). Under idealized inverse barometer conditions, changes in atmospheric pressure would not be observable in the bottom pressure; the pressure from the water column would be reduced by an amount equal to the increase in the atmospheric pressure. It is thus tempting to neglect atmospheric pressure when computing depths from measured pressure. While atmospheric pressure clearly has an effect on the *instantaneous* actual depth of a pressure sensor, under inverse barometer conditions it would not affect the depth calculated from the sensor relative to some stable datum like MSL. We include atmospheric pressure effects here for two reasons: significant departures from inverse barometer response have been observed - particularly in the tropics (Mathers and Woodworth, 2004); and the Gibbs Seawater (GSW) equations are strictly valid only for standard atmospheric pressure.

The GSW calculations are based on standard reference sea level pressure of 101,325 Pa. We subtract the observed barometric pressure from the pressure records at all depths. This gives us a more accurate calculation of the instantaneous height of the water-column above the sensor. The effect of the perturbations of atmospheric pressure on the water surface relative to MSL are accounted for in our case by the water-level correctors and associated datum realization. Including the atmospheric correction in the water-level based datum reduction method may be problematic if the reference station is far relative to typical atmospheric pressure gradients or if the departure from the inverse barometer effect (or the transfer function between atmospheric pressure and water-level) were different between the survey location and the controlling gauge.

This correction of water levels for atmospheric loading would also not be applied under the inverse barometer assumption if the water-level corrections were done only with a harmonic tide model but should generally be applied if ellipsoid based positioning (e.g., GNSS) of the water surface were used. To expand on this, consider a location in the ocean that behaves as a perfect inverse barometer. A pressure sensor in a fixed location relative to MSL would not see any pressure change under a change in atmospheric loading. A purely harmonic model of tides does not include any short-term pressure variations effects, so atmospheric pressure can safely be neglected under these conditions. If the instantaneous sea-surface is measured relative to a stable datum (e.g., by a GNSS buoy) and the sea surface responds to atmospheric loading, the apparently fixed pressure-derived depth must be corrected for changes in atmospheric pressure such that the sum of the pressure-derived depth and the distance of the water surface to the datum remains constant.

If a given location in the ocean does not behave in accordance with the inverse barometer effect, application of harmonic tide models will generally have some error from the atmospheric pressure. Full correction of the atmospheric pressure effect is equivalent to assuming there is no effect on the water surface from atmospheric loading, while no correction is equivalent to assuming an ideal inverse barometer effect. When the actual instantaneous water level is positioned using GNSS or a nearby water level gauge, atmospheric pressure should be removed from the pressure record, and whatever effect that loading has on the water surface will be captured by the water level measurement.

During the dives, the variation of atmospheric pressure from standard atmospheric pressure was small (~0.04 dbar). However, this will not always be the case. For all of 2015 at Guam, there were nine instances of deviation larger than 0.10 dbar and one larger than 0.25 dbar. The largest are associated with passing tropical cyclones. If uncorrected, this surface pressure variation will couple directly to depth errors where we can approximate the depth error in meters as the pressure variation in dbar, subject to the inverse barometer discussion above. For this work, the atmospheric contribution to the overall error is small, but in shallow water the atmospheric pressure correction may be a substantial

fraction of the total error.

4. Results

4.1. Measured CTD profiles

During this expedition, there were 18 lander deployments over 12 operational days spanning June 6 to June 26, 2020. The submersible was deployed on six of these days. Of the lander deployments, we rejected six CTD profiles that had unrealistic absolute salinity values greater than 40. Using these measured profiles and an assuming a reference pressure of 11,260 dbar (corresponding to a depth of approximately 10,930 m), we calculated the depth using each profile. The standard deviation of the calculated depths was 17 cm. This is not substantially larger than our expected measurement uncertainty of 11 cm which may indicate that we did not observe any variability other than measurement noise. Accordingly, we used a single profile from June 26 to process all dives.

4.2. Dive results

Profiles of the seafloor for the six dives are shown in Fig. 7. The dives were planned as transects over the deepest areas of each basin as identified by surface mapping. Aside from the location of the submersible descent, ascent, and lander tie points (based on the deployment location of the lander), there was no horizontal positioning of the submersible. The x-axis is time in seconds (UNIX POSIX seconds in UTC). The horizontal velocity of the submersible along the seabed changed with time (possibly even reversing directions occasionally), so this scale cannot be unambiguously tied to a distance metric. We use the mapping results from Bongiovanni et al. (2021) on the accompanying geographic plots (Fig. 8) to generally locate the dive profiles. We show the submersible surface deployment position, lander deployment position, and approximate path the submersible travelled on the seafloor. During the June 12 dive, the submersible came within 150 m of the lander but did not actually co-locate with it. We have used the closest point of approach as a tie-point for this dive.

4.3. Uncertainty analysis

The spread in the RBR pressure gauges indicates that the operational accuracy of these instruments is lower than the pre-deployment calibration suggested but well within the specified accuracy of the instruments. We use the standard deviation of the average difference of the RBR gauges when deployed together to estimate 1-sigma uncertainty of 2 m from the pressure gauges. The residual surface offset was well less than this for all dives. The unaccounted-for drifts in the instruments add up to an additional meter of uncertainty from the pressure measurement when far in time from a tie point. Though this is not a random effect, we account for it by increasing the pressure sensor uncertainty to 3 m. The next largest source of uncertainty is the gravity correction, which we have estimated at ±0.5 m. This is admittedly a bit of a guess, though we showed in section 3.3.2, Gravity at Depth, that it should be considerably smaller than 2 m by considering bounding cases for the gravity model. The CTD measurement uncertainty is 0.11 m and the measured variation in the water column is 0.17 m, though these last two figures may be different manifestations of the same root uncertainty. Finally, water level uncertainty is 0.08 m and atmospheric pressure uncertainty is negligible in this case. Thus, the root-mean square 1-sigma uncertainty is 3 m (6 m at 95% C.I.) and is dominated by the pressure sensor uncertainty (Table 3).

4.4. Deepest depth

Each dive was planned over the deepest section of the three basins using the mapping data of Bongiovanni et al. (2021). With the exception of the June 26 dive, we used a RBR pressure gauge on a lander to establish the depth of the seafloor at the lander relative to mean sea level (MSL). We tied the seafloor profile from the submersible altimeter into this datum using the recorded time of rendezvous between the submersible and lander. Much like a land surveyor tying into a local benchmark, this allowed us to transfer the vertical control from the static lander deployment to the vehicle and subsequently to the altimeter records along the entire profile. On June 26, we used a RBR sensor on the vehicle to vertically control the profile as described in section 2.2. The submersible traveled along the transect at variable heights of a few meters above the seafloor, but using the altimeter combined with the onboard pressure sensors and the established vertical control, we are able to reference this seafloor profile to MSL.

The deepest seafloor depths were found in the south-east portion of the eastern basin. The June 7 and 12 dives showed a maximum depth of 10,932 m though neither crossed the deepest area indicated by surface mapping from Bongiovanni et al. (2021). The June 14 and June 26 dives did cross the deepest area of the eastern basin indicated by surface mapping. The maximum depth of the June 14 dive 10,936 m. This was observed approximately 30 min after the lander tie-point, so it is likely this measurement is biased deep due to CTD pressure drift by ~ 0.25 m. On the June 26 dive, the maximum depth was 10,934 m. Due to the unaccounted for RBR drift for this dive, this depth is likely biased up to a meter shallow.

The one dive in the western basin, on June 20, observed a maximum depth of 10,933 m. This depth was observed almost an hour after the tie-point, so may be biased up to 0.5 m deep by the CTD pressure sensor drift. The deepest point was along the northern extent of the basin immediately adjacent to the northern wall of the trench. The one dive in the central basin observed a maximum depth of 10,922 m. This was in the vicinity of the deepest area determined by surface mapping.

Based on these results, we estimate the maximum depth of the Challenger Deep to be located in the eastern basin at approximate position 11° 22.4′N, 142° 35.6′ E and a depth of 10,935 ± 3 m at 1-sigma (±6 m at 95% C.I).

5. Discussion

5.1. Comparison with other reported depths

As for the location of the deepest depth being in the eastern basin, this study agrees with the deepest location determined by Nakanishi and Hashimoto (2011) using multibeam sonar. Nakanishi and Hashimoto (2011) estimated a depth uncertainty of 5 m (at 95% C.I.) from the internal consistency of a number of largely contemporaneous soundings. Because their estimate takes no account of the common sources of error in these sounding (e.g., the sound speed profile), the uncertainty is almost certainly too low. The more rigorous estimate of depth uncertainty by Gardner et al. (2014) of 25 m (at 95% C.I.) for a similar system is probably more representative for acoustic work from surface ships. Using this larger uncertainty figure, our depth results are consistent with Nakanishi and Hashimoto's (2011) reported depth of 10,920 m. The deepest depth we calculated in the western basin was very nearly as deep as the eastern basin, and our results are consistent with Van Haren et al.'s (2017) measurement there of 10,925 ± 12 m (at 95% C.I.). Our results are also consistent with the deepest depth of 10,924 ± 15 m (at 95% C.I.) measured by Bongiovanni et al. (2021) in the eastern basin. We do not agree with Garner et al.'s (2014) estimate for the western basin (10,984 ± 25 m at 95% C.I.), the Loranger et al. (2021) estimate for the central basin of 10,983 ± 12 m (at 95% C.I.), or the Taira et al. (2005) estimate for the eastern basin (10,989 m with no reported uncertainty). This study had only one dive in the western and central basins, and the dive profiles do not cross the location of these deeper depth estimates in those basins. However, it seems unlikely that the either basin contains an undetected depression nearly 60 m deep.

Comparing to other submersible-based observations, Gallo et al.

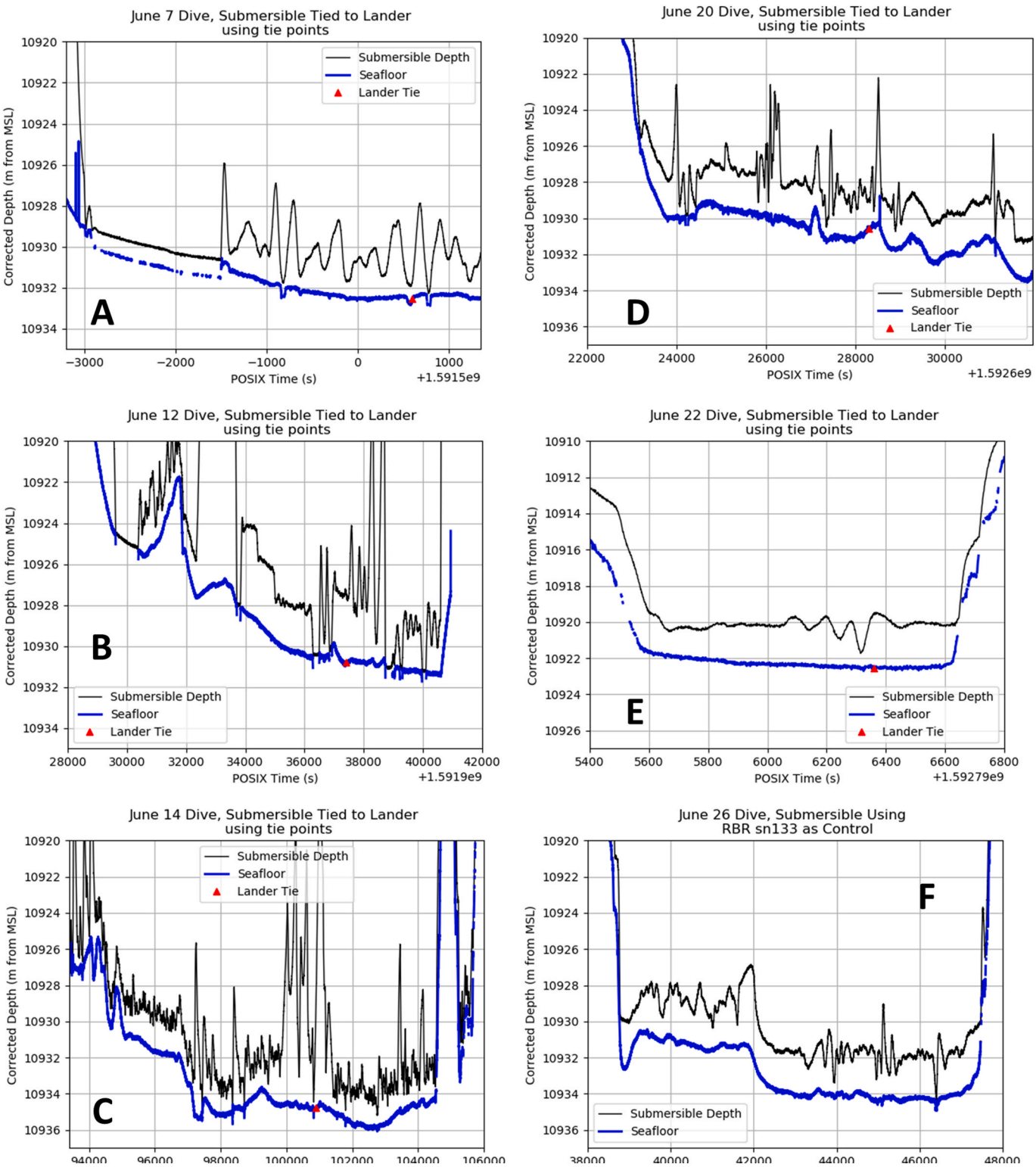

Fig. 7. Vehicle depth and seafloor profiles. Where the submersible approaches the seabed, thruster wash or penetration into the sediment shows as short vertical artifacts in the bottom profile. A: June 7, Eastern Basin. The segment of the profile from −3000 to −1500 s is the submersible stationary on the seafloor. The drift in the CTD controlled depth is apparent. During this segment, the altimeter is reporting weak returns from ~1 m below the surface. Maximum seafloor depth 10,932 m. B: June 12, Eastern Basin. Maximum seafloor depth 10,932 m. C: June 14, Eastern Basin. Maximum seafloor depth 10,936 m. D: June 20, Western Basin. Maximum seafloor depth 10,933 m. E: June 22, Central Basin. Note the different vertical scale in the profile. Maximum seafloor depth: 10,922 m. F: June 24 June 26, Eastern Basin. This dive was vertically controlled with the RBR sensors mounted on the vehicle rather than establishing a reference datum with the sensor on the lander. Maximum seafloor depth: 10,934 m.

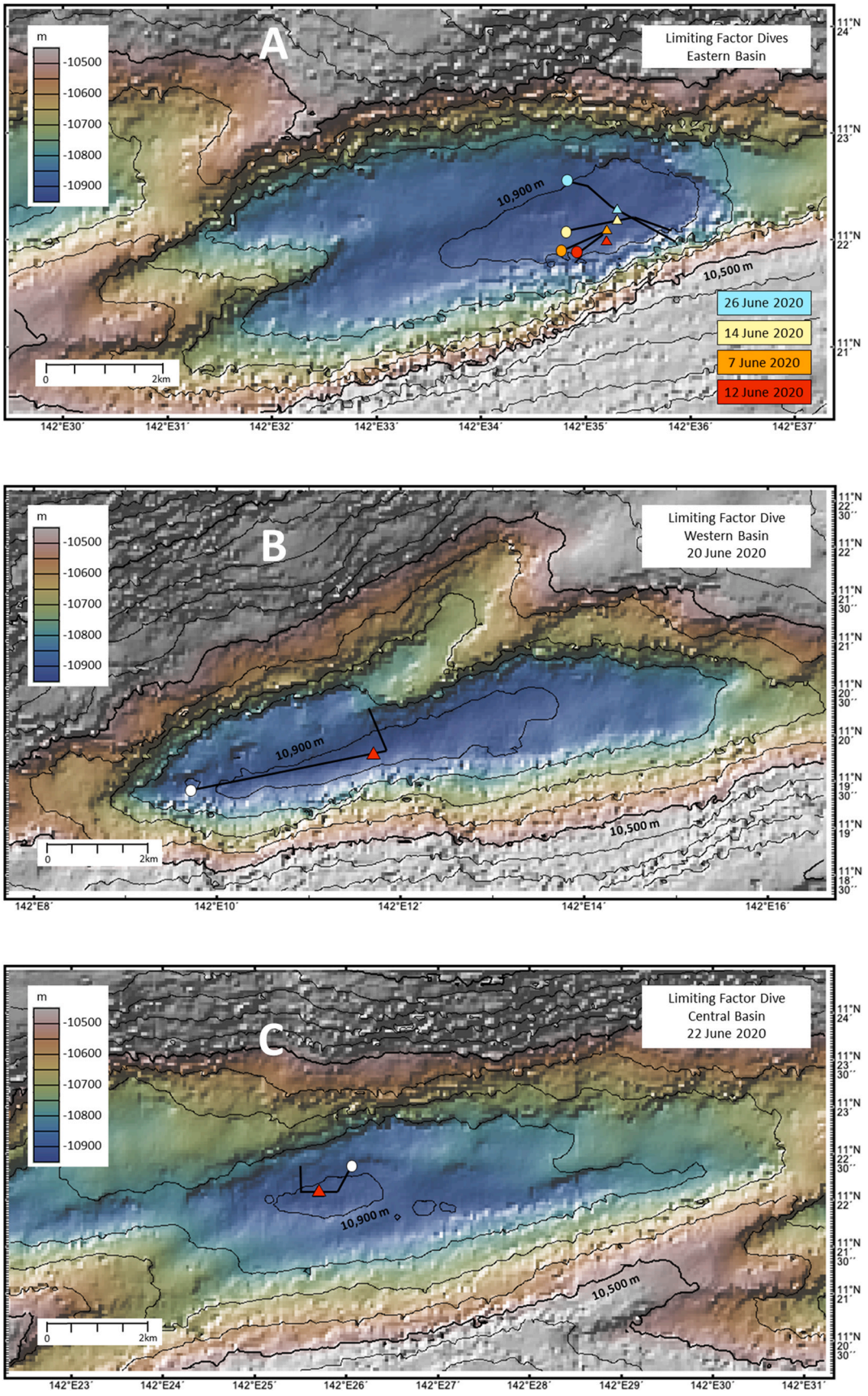

Fig. 8. Approximate tracks of dive profiles in eastern (A), central (B), and western (C) basins. Circles indicate decent location and triangle show rendezvous with lander. Background bathymetry from Bongiovanni et al. (2021).

Table 3
Contributions to depth estimate and associated uncertainty.

	Depth Contribution (m)	Uncertainty (m)
pressure sensor and correction for standard ocean	10,922	3
CTD measurement and correction for dynamic height anomaly	8.7	0.11
gravity and gravity gradient correction	4.2	0.5
CTD temporal variability	na	0.17
water levels	<0.5	0.08
atmospheric loading	<0.1	0
Total	10,935	3 (RMS)

(2015) reported a maximum depth of 10,908 ± 3 m (presumably at 1-sigma) for the *Deepsea Challenger* in the eastern basin and 10,918 ± 3 m for an un-crewed lander in the central basin. The reported position of the *Deepsea Challenger* dive is consistent with the position of the deepest position found with this study, but the depth is 27 m shallower. It is possible Gallo et al. did not correct for the dynamic height anomaly when applying the UNESCO equation, which would not be unusual in general oceanographic practice. This would account for 8 m of the difference, and our additional correction for gravity would account for another 4 m, leaving a difference of 15 m unexplained. Based on the dive location and Gallo et al.'s description of the transect along the seafloor, it seems unlikely that the vehicle was not in the basin proper.

Trieste dove in the western basin, but positioning was relatively crude by modern standards. Prior to the dive, the deepest location was sounded by a support ship using TNT and marked with flares (Piccard and Dietz, 1961). Additionally, overall positioning of the mission in a global frame would have likely used celestial navigation. Depending on the latest good celestial fix, the position uncertainty of the surface ships could have been many km. The position uncertainty was not discussed by Piccard and Dietz. Given the position uncertainty as well as the fact that the *Trieste* did not maneuver along the seafloor, the results here are consistent with the Piccard and Dietz reported depth of 10,910 m.

5.2. Could it be the sound speed?

Van Haren (2017) suggested that the discrepancies between their results and other acoustic measurements (e.g., Gardner et al., 2014, Taira et al., 2005) were due to differences in sound speed profiles. In a similar vein, Taira et al. (2005) corrected the reported 1957 depth from the *Vityaz* from 11,035 m to 10,983 m by backing out the original sound speed correction and applying one from their measured CTD profile. We compare sound speed profiles as well as the sound speed equations used in this section. We were able to obtain the profiles used by Taira et al. (2005), Gardner et al. (2014), van Haren et al. (2017), and Loranger et al. (2021). We found that the profiles and differences in the sound speed equations used are insufficient to account for the differences in the reported maximum depth.

The sound speed profile is a critical part of any acoustic measurement. For multibeam systems with oblique ray paths through the water column, refraction is a concern and generally a ray-tracing correction is needed to correctly position the sounding on the seafloor (Beaudoin et al., 2009). However, within an angle of ±45° from nadir, the greatest vertical depth uncertainty due to uncertainty in the sound speed profile is at nadir. For this analysis, we assume that the reported greatest depths came from nadir or near nadir soundings and focus on the harmonic sound speed rather than ray-tracing approaches. Applying an average sound speed that is faster than what is physically in the water column will yield a calculated depth sounding that is deeper than the actual depth.

Taira et al. (2005) used contemporaneous CTD profiles to correct the readout depth of the sounder. They did not specify the sound speed equation used, but presumably used Chen-Millero (Millero et al., 1980), consistent with the UNESCO equation they used to calculate density. We were unable to obtain the profile used by Nakanishi and Hashimoto (2011). Gardner et al. (2014) measured temperature to depth of 800 m to 1000 m with an expendable bathythermograph (XBT) and used a U.S. Naval Oceanographic Office database for salinity values and to extend the measured profile to the seabed. They used the Chen-Millero (Millero et al., 1980) sound speed equation (A. Armstrong, personal communication, June 24, 2020). Van Haren et al. (2017) used a contemporaneous profile to 8,000 m, measured with a CTD lowered on a wire rope, and used the Del Grosso equation (Del Grosso, 1974) to calculate sound speed. Loranger et al. (2021) estimated a depth using a contemporaneous profile made with a free-fall profiler and the Del Grosso equation.

For comparison, we calculated the sound speed profile for each CTD deployed on a lander during this expedition using the TEOS-10 sound speed formula (Table 4). We also calculated the difference in depth using the Lander CTD as a reference and a reference depth of 10,934 m. That is, we calculate what the reported depth difference would be for each profile assuming the true depth were 10,934 m and the true harmonic mean were 1,554.1 m/s. Gardner et al. (2014) used the fastest profile, but the profile could account for up to 13 m of the difference at this depth (Table 4). Recall that the depth from Gardner et al. (2014) was 50–60 m deeper than the estimate of van Haren et al. (2017) or this paper. For a representative profile at the Challenger Deep, the Del Grosso and TEOS-10 formula are equivalent and Chen-Millero is slightly faster, accounting for a 5-m difference at this depth (Table 5).

Based on this analysis, neither the sound speed profiles used nor the sound speed equation explain the difference in depth (approximately 50 m) between the depths in the vicinity of 10,980 m reported by Taira et al. (2005), Gardner et al. (2014), and Loranger et al. (2021) and those in the vicinity of 10,920 reported by Nakanishi and Hashimoto (2011), van Haren et al. (2017), and Bongiovanni et al. (2021).

It is possible that the sound speed of the deep ocean is incorrect in all the models, but this would not explain the discrepancy between acoustic mapping missions. It is also possible that the density estimated from the TEOS-10 model used here (and the UNESCO equation that predated it) is incorrect in the deep ocean, which would skew all pressure-derived results. We think it is more plausible that the results in the vicinity of 10,980 reflect unknown instrument configuration inaccuracies, noise, or other factors. Non-nadir returns would seem to have a possibility of biasing the results of the implosion-echo method used by Loranger et al. (2021), particularly in light of the observation that their reported position is not coincident with the deepest position of any of the basins indicated by surface mapping.

6. Future work

The pressure sensor used here dominated our overall uncertainty. While 3 m of uncertainty in nearly 11 km is remarkable, more accurate pressure sensors are available or under development. Controlling or

Table 4
TEOS-10 Harmonic sound speed and impact on calculated depth using a reference depth of 10,930 m and the profiles from this paper as a reference.

Mission	Number of Profiles	Harmonic Mean (m/s)	Standard Deviation (m/s)	Depth Difference (m)
This paper	18	1,554.1	0.14	0
Taira et al. (2005)	3	1,552.9	0.24	−8
Gardner et al. (2014)	5	1,555.8	0.5	13
van Haren et al. (2017)	1	1,553.3	N/A	−5
Loranger et al. (2021)	1	1,552.9	N/A	−8

Table 5
Effect of different sound speed equations. Depth difference calculated depth using a reference depth of 10,930 m and the profiles from this paper as a reference.

Formula	Harmonic Mean (m/s)	Depth Difference (m)
TEOS-10	1554.1	0
Del Grosso	1554.1	0
Chen-Millero	1554.8	+5

correcting for instrument drift will be critical. The method used here of establishing depths at fixed sites and then tying in the submersible to those depths was useful to determine instrument drift and validate the application of other correctors. With improvements to the pressure measurement, gravity will come to dominate the error. For absolute accuracies of under a meter in the deep trenches, we will need more sophisticated modeling of the downward propagation of gravity at the measurement location. Ideally, we would augment a gravity modeling effort with direct measurements using a gravimeter. Unlike many instruments deployed in the sea, a gravimeter could make the required measurements while fully within the confines of a pressure housing. To achieve sub-meter accuracies, we will also need to abandon the approximation of using pressure in the gravity equation and directly calculate the average gravity over the column to figure the depth from the integrated dynamic height. This effort may not be required for areas with relatively benign gravity variations, such as the abyssal plains. Following gravity, measurement of the water properties could be improved. For hadal depths, we found the pressure sensor of the CTD sensor to be limiting. Aside from improving the CTD pressure sensor, another approach might be to couple measurements made in the upper portion of the column with a CTD rated to only a few hundred meters with mid and full ocean depth profiles. Because the pressure sensor accuracy is a portion of the full scale, the combined profile would be more accurate than a single, full-depth profile. These shallow profiles would also be much easier to take and might better capture any variability near the surface. For this work, we were fortunate to have a long-term pressure sensor deployment to reference water levels. Generally, we will need either modeled water levels at the measurement location or we will need to directly position the water surface (e.g., with a GNSS buoy) and then apply a datum model to bring measurements to our datum of choice. With these improvements, pressure-based depth measurements in any part of the world's ocean at sub-meter absolute accuracy seem achievable.

The profiles of the seafloor at the bottom of the ocean shown in this report are tantalizing. It is clearly not a flat and featureless terrain and complete bathymetric coverage at meter or submeter horizontal resolution would undoubtedly be of interest. Mapping these depths with instruments on surface ships is limited to horizontal resolutions of hundreds of meters. A higher-resolution mapping mission would require integration of a hadal depth-rated multibeam mapping system into a deep submergence vehicle. This would be non-trivial. A deep mapping effort could leverage the approaches in this paper for vertical control.

We do think that the transects across the basins shown in this report, controlled by direct pressure observations and accounting for steric, gravity, and water-level effects, are the most comprehensive, precise, and accurate estimates of the depth of the Challenger Deep, and thus the maximum depth of the ocean, to date.

Declaration of competing interest

The authors declare that they have no known competing financial interests or personal relationships that could have appeared to influence the work reported in this paper.

Acknowledgements

We are grateful to Chris Meinig of NOAAs' Pacific Marine Environmental Laboratory for many useful discussions on deep sea pressure measurements and Walter H.F. Smith of NOAA's Laboratory for Satellite Altimetry for many long and fruitful exchanges on gravity in the ocean. The team at Caladan Oceanic, specifically Victor Vescovo, Cassie Bongiovanni, and Tim Macdonald, very generously shared information and data, and fully supported following the science in this effort. David Wolcott at NOAA's Center for Operational Oceanographic Products and Services helpfully performed the tide-by-tide comparison.

Appendix A. Pressure to Depth Calculations

A.1 The Hydrostatic Equation

The application of the hydrostatic equation here is not new, but because of the different implementations of a reference pressure level, different definitions of heights in the literature, and other considerations, it is worth building the equations from basic principles. This derivation largely follows that in the TEOS-10 manual (TEOS-10; IOC, SCOR and IAPSO, 2010) with some clarification.

Consider a small box of water of cross-sectional area A, height Δh, and density ρ in the earth's gravity g. The gravitational force on this box, its weight, is:

$$F = mg = A\Delta h\rho g \tag{A.1}$$

The weight of this box then exerts a pressure, a force per unit area on the bottom surface, where the increase in pressure from the top of the box to the bottom is:

$$\Delta p = \frac{F}{A} = \frac{A\Delta h\rho g}{A} = \rho g\Delta h \tag{A.2}$$

Considering a stack of such boxes forming a column of water, the total pressure of the column is a sum across the boxes. If the density and gravity of the column can be considered constant, Eqn A.2 is sufficient to calculate depth from pressure, and this is how typical shallow water depth gauges, such as those used by scuba divers, work. For precision work, we need to consider that density and gravity vary along the water column. Because density is a function of pressure and gravity is in general a function of height, this equation is conveniently rearranged to:

$$\frac{1}{\rho}\Delta p = g\Delta h \tag{A.3}$$

The inverse of the density is known as the specific volume, α. Letting the increments go to infinitesimal differentials and integrating along the column gives:

$$\int_0^P \alpha \, dp = \int_0^H g \, dh \tag{A.4}$$

The density and specific volume of seawater is a function of pressure, temperature, and dissolved minerals, predominantly salts. The specific volume of seawater is often written as the sum of the specific volume of the standard ocean (seawater at temperature of 0 °C and reference salinity of 35 on the Practical Salinity Scale PSS-78) and the specific volume anomaly, δ.

$$\alpha = \alpha_0(T = 0, S = 35, p) + \delta(T, S, P) \tag{A.5}$$

This is done so that the first term, α_0, is a function only of pressure while the density effects of temperature and salinity are restricted to the second term, δ.

$$\int_0^P a_0 \, dp + \int_0^p \delta \, dp = \int_0^H g \, dh \tag{A.6}$$

These integrals yield potentials typically referred to in both the oceanographic and geodetic communities as a *dynamic height*. The integral of the specific volume anomaly, the second term of the left side of Eqn A.6, is called the *dynamic height anomaly* or the *geopotential anomaly* (IOC, SCOR and IAPSO, 2010). The units of dynamic height and dynamic height anomaly are m^2/s^2. The right side of Eqn A.6 is equivalent to an average gravity over the column multiplied by the height.

$$\int_0^P a_0 \, dp + \int_0^p \delta \, dp = \overline{g} H \,, \quad \overline{g} = \frac{1}{H} \int_0^H g \, dh \tag{A.7}$$

Conversely, the dynamic height divided by the average gravity gives the height (or depth) of the column. This is the relationship we use to calculate depths from observed pressures. We use depth as a positive quantity throughout this report.

$$\frac{\int_0^P a_0 dp + \int_0^P \delta \, dp}{\overline{g}} = H \tag{A.8}$$

A.2 Pressure to Depth, A Comparison of Linear Models, the UNESCO equation, and TEOS-10

One convenient and common approximation to derive depth from observed pressure is to use the pressure in decibar (dbar) as equivalent to the depth in meters. One bar is defined as 10^5 Pa, so 1 dbar is equal to 10^4 Pa. Treating one dbar as equal to a depth of 1 m is equivalent to approximating g = 10 m/s^2, and ρ = 1 g/cm^3, or g = 9.81 m/s^2 and ρ = 1020 kg/m^3. For some applications in shallow seawater, this approximation is often accurate enough, but yields errors of 50 m (too deep) in 4 km of sea water and 300 m (again too deep) at 11 km (Figure A1, left panel). The compressibility of seawater is the dominant part of this discrepancy. A formulation of Eqn A.8 by Saunders and Fofonoff (1976) and later refitted by Fofonoff and Millard (1983) to the 1980 Equation of State of Seawater (EOS-80) is commonly used in oceanography and is typically known as the "UNESCO pressure to depth" conversion or simply, the "UNESCO equation". Many authors (e.g. Diez, 2017; IOC, SCOR and IAPSO, 2010) purposely neglect the dynamic height anomaly when using the UNESCO equation. This is equivalent to assuming the water column is made up of standard ocean (seawater at temperature of 0 °C and salinity of 35 on the Practical Salinity Scale PSS-78), in effect discarding any information on the temperature or salinity of the column. This assumption of a standard ocean is not as egregious as it may seem, and results in a contribution to the depth error of less than 10 m even for the deepest depths considered here.

The international Oceanographic Commission approved replacing EOS-80 with a new International Thermodynamic Equation of State of Seawater 2010) (TEOS-10) in 2009. We use the TESO-10 model (IOC, SCOR and IAPSO, 2010) and the associated Gibbs Seawater Toolbox (GSW) (McDougall and Barker, 2011) throughout this report. The difference in pressure to depth determinations between TEOS-10 and UNESCO equation for standard seawater at latitude 11 N is shown in the right panel of Figure A1. The difference between the two equations for the standard ocean less than 10 cm at all depths.

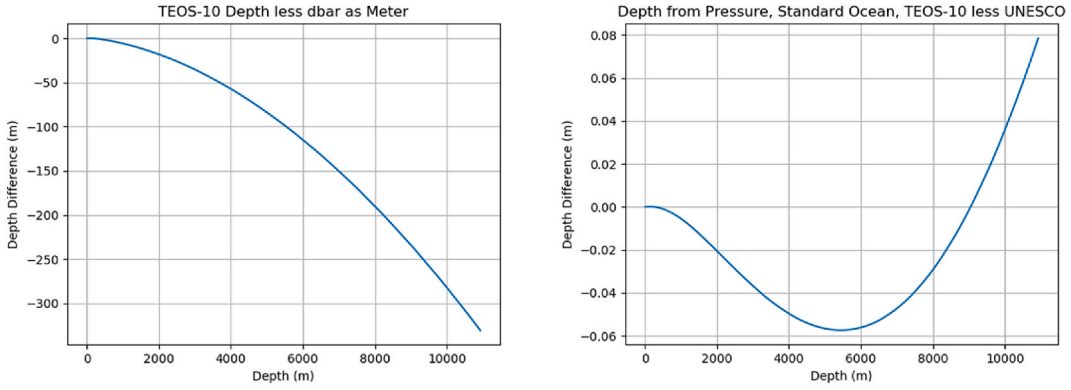

Fig. A1. Difference between TEOS-10 and 'decibar-as-meter' (left) and UNESCO equation (right).

A typical profile for conditions at the Challenger Deep is shown in Figure A2.

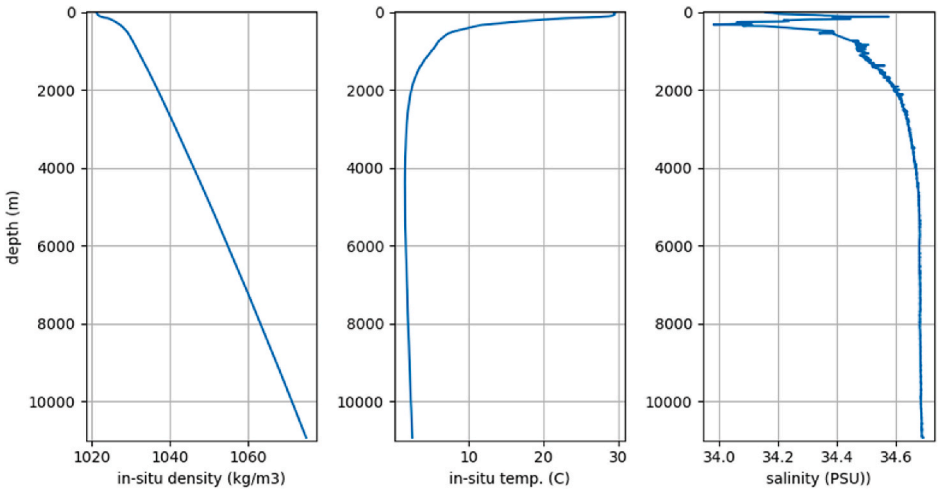

Fig. A2. In-situ density (left), in-situ temperature (middle), and salinity (right) for a typical CTD profile for this project. This is from a June 26 lander deployment.

Using the profile shown in figure A2, we compared depths calculated with the measured salinity and temperature against using the standard ocean for all depths (Figure A3). Depths calculated using the dynamic height anomaly from the CTD profile are 8 m deeper at 10,000 m than using the standard ocean (i.e., ignoring the dynamic height anomaly) because the ocean at this location is less dense than the standard ocean.

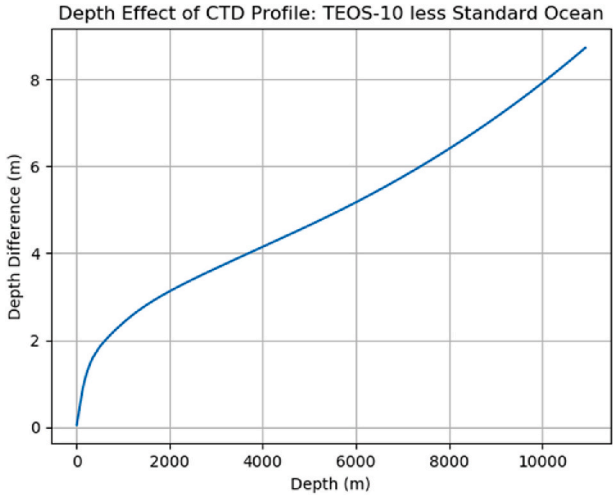

Fig. A3. (left) Difference between TEOS-10 depth calculations using full CTD profile (i.e., applying dynamic height anomaly) and TEOS-10 calculations assuming standard ocean (i.e., neglecting dynamic height anomaly), UNESCO standard ocean, and TEOS-10 depth with bottom salinity and temperature assumed for full profile.

For any particular location, the difference between a depth calculated assuming a standard ocean and using a measurement of the actual density of the ocean will depend on how different the ocean is from the standard ocean, but in general, the difference is surprisingly small. This is the converse of why CTD profiles of salinity and temperature as a function of pressure are so effective at measuring the small changes in potential that drive geostrophic flows.

Appendix B. Gravity in the Sea

B.1 Surface Gravity

If the earth were a uniform, non-rotating spherical mass, gravity would be a constant magnitude over the surface. However, the rotation, non-spherical nature, and uneven mass distribution of the earth cause substantial variation of gravity with location. To account for the rotation and non-spherical nature of the earth, both the UNESCO pressure to depth equation and TEOS-10 toolbox use the ellipsoid based GRS 80 gravity model (Moritz, 1980) for the surface gravity as a function of latitude, φ. The GRS 80 gravity model assumes the earth is a uniform, rotating ellipsoid. The closed form of this ellipsoid gravity model is:

$$g_{GRS80} = g_e\left(\frac{1+k\sin^2\varphi}{\sqrt{1-e^2\sin^2\varphi}}\right) \; with\; k = \frac{bg_p}{ag_e} - 1 \tag{B.1}$$

where g_e is the normal gravity at the equator, g_p the normal gravity at the pole, b is the semi-minor axis, a is the semimajor axis, and e is the first eccentricity.

This closed form can be expanded in series form to:

$$g_{GRS80}(\varnothing) = 9.780327\left(1 + 5.2790 \text{ x } 10^{-3}\sin^2\varphi + 2.32 \text{ x } 10^{-5}\sin^4\varphi + \ldots\right) \tag{B.2}$$

This is the surface gravity term in both the UNESCO and TEOS-10 pressure to depth conversions. The gravity at the pole is about 0.5% higher than the gravity at the equator. Failure to account for this variation with latitude could result in errors of up to 5 m for every km of depth.

While this ellipsoid model is an improvement on the spherical earth, the actual mass distribution on the earth is not uniform. The result is deviations from the GRS 80 modeled gravity at the surface. Gravity anomalies are typically reported in units of mGal. A gal is defined as a cm/s^2, so a mGal is equivalent to 10^{-5} m/s^2. While typical surface gravity anomalies are ±50 mGal (RMS value for terrestrial and near coastal points as calculated by Hirt et al., 2013), the gravity anomalies are much larger in some areas, particularly above the deep ocean trenches.

B.2 Gravity at Depth

For clarity, we present a simple derivation of the vertical gradient of gravity in the sea using a non-rotating, spherical earth model and justify neglecting the rotation and ellipsoid nature of the earth. In the supporting documentation for the TEOS-10 manual, McDougal (2010) provided a slightly different derivation for the gravity gradient in support of the formulations used in TEOS-10. McDougal also noted that the numerical value of the gravity gradient implemented in both the TEOS-10 and UNESCO formula were originally presented by Saunders and Fofonoff (1976) with no derivation or supporting references. Because it is so simple, the derivation below is likely not original and is very similar to the approach used by Airy (1856). However, the only derivations we can find in the literature are confused between application and approximations (e.g., Karl, 1971); assume a constant density with depth (e.g., Airy, 1856; Karl, 1971; McDougal 2010); or use a more complicated ellipsoid model of the earth (e.g., Dahlen, 1982). We think including this derivation here is useful both to better generally understand the origin of the gravity gradient in the sea but also because we use our derived results to model end-case approximations of the gravity field at the Challenger Deep.

Consider a spherical earth comprised of shells of uniform density, ρ, that vary with depth. The gravity at the surface of the earth is:

$$g_0 = \frac{m_e G}{R_0^2} \tag{B.3}$$

where m_e is the mass of the earth, G is the universal gravitational constant, and R_0 the radius of the earth. As we go below the surface of the earth, or descend into the ocean, the effective mass of the earth beneath us is reduced. As shown by Newton (1687), the gravitation attraction inside a spherical shell is zero, so we can neglect the gravitational attraction of the shells above us and just calculate the gravitational attraction of the diminishing mass of earth beneath us. The mass of a thin shell of thickness dr at a radius r from the center of the earth is:

$$m_s = 4\pi r^2 \rho(r) dr \tag{B.4}$$

The mass of a number of shells from the surface to some depth, $d = R_0 - r$, is:

$$m_S = 4\pi \int_{R_0-d}^{R_0} \rho(r) r^2 dr \tag{B.5}$$

Changing the variable to d from r:

$$m_S = 4\pi \int_0^d \rho(d)(R_0 - d)^2 dd \tag{B.6}$$

or

$$m_S = 4\pi \int_0^d \rho(d) {R_0}^2 \left(1 - \frac{2d}{R_0} + \frac{d^2}{{R_0}^2}\right) dd \tag{B.7}$$

We can then write the gravity (Eqn B.3) at some depth as

$$g(d) = \frac{(m_e - m_S)G}{(R_0 - d)^2} = \frac{(m_e - m_S)G}{{R_0}^2\left(1 - \frac{d}{R_0}\right)^2} \tag{B.8}$$

Expanding using Taylor series gives:

$$g(d) = \frac{(m_e - m_S)G}{{R_0}^2}\left(1 + \frac{2d}{R_0} + \ldots\right) \tag{B.9}$$

Combining Eqn B.7 and Eqn B.9 and simplifying gives the exact solution (if we keep the higher order terms of the expansion):

$$g(d) = \left[g_0 - 4\pi G\overline{\rho} d - 4\pi G \int_0^d \rho(d)\left(-\frac{2d}{R_0} + \frac{d^2}{{R_0}^2}\right) dd\right]\left[1 + \frac{2d}{R_0} + \ldots\right], \text{ where } \overline{\rho} = \int_0^d \rho(d) dd \tag{B.10}$$

If $\frac{d}{R_0}$ is small, terms multiplying G and $\frac{d}{R_0}$ will be very small, so by setting all terms with $G\frac{d}{R_0}$ to zero, the gravity as a function of depth is approximately:

$$g(d) \cong \left[g_0 - 4\pi G\overline{\rho} d + \frac{2dg_0}{R_0} \right] \tag{B.11}$$

or

$$g(d) \cong g_0[1 + \gamma d] \tag{B.12}$$

with

$$\gamma = (F_S - B_S)\ F_S = \frac{2}{R_0}\ B_S = \frac{4\pi G\overline{\rho}}{g_0} \tag{B.13}$$

where B_S is the term typically referred to as the *Bouguer* term and F_S is the spherical *free-air* term. Note that the density in the Bouguer term is the average density between the surface and the depth of interest. The Bouguer correction has caused confusion in the literature (e.g., Karl, 1971) due to a lack of clarity if the calculation is being used to *remove* the gravitational effect of known topography above the point of interest (where the factor is 2π) as opposed to calculating the effect of *tunneling through* a layer that is figured to have been left in place to calculate the in-situ gravity (where the factor is 4π as it is here).

For a constant seawater density of 1,028 kg/m^3, $G = 6.6743 \times 10^{-11}$ (Newton's gravitation constant in SI units), and using a value of for the radius of the earth, R_0, of 6.378×10^6 m, the combination of the Bouguer term and the spherical free-air term gives a $\gamma = 2.26 \times 10^{-7}$ 1/m or a gravity gradient of $\gamma g_0 = 2.21 \times 10^{-6}$ 1/s^2 or 2,210 Eötvös (E, 1E = 1x10^{-9} 1/s^2). Thus, the nominal gravity gradient in the sea is 2,210 E. This is the value used in both the UNESCO and TEOS-10 formulations, such that in both, gravity as a function of depth and latitude is taken as:

$$g(\varnothing, d) = g_{GRS80}(\varnothing)[1 + \gamma d] \tag{B.14}$$

where the g_{GRS80} is given in equation g2 and is γ is 2.26×10^{-7} 1/m.

In deriving the gravity gradient, we have ignored the both the rotation and non-spherical nature of the earth. We can neglect the rotation in calculating the gravity gradient because the change in centripetal acceleration with depth is small (a maximum of 5E at the equator: centripetal acceleration = $a_c = \omega^2 r$, $da_c/dr = \omega^2 = 5E$ using the earth's sidereal rotation rate $\omega = 7.2 \times 10^{-5}$ radians/s). We can also neglect the non-spherical nature of the earth in calculating the gradient because this too has a small effect. Gravity as a function of depth for a model of the earth consisting of ellipsoid shells of constant density was described by Dahlen (1982), but calculations based on this model show that the difference from the spherical model over 11 km of depth is on the order of 10E, and thus small compared to other factors. (W.H.F. Smith, personal communication, 2020).

CRediT author statement

Samuel F. Greenaway: Methodology, Formal analysis, Visualization, Writing – Original Draft. **Kathryn D. Sullivan**: Conceptualization, Writing - Review & Editing, Data Curation. **S. Harper Umfress:** Formal analysis, Data Curation, Writing - Review & Editing. **Alice B. Beittel:** Formal analysis, Data Curation, Visualization, Writing - Review & Editing. **Karl D. Wagner:** Formal analysis, Data Curation, Writing - Review & Editing.

Funding

This research did not receive any specific grant from funding agencies in the public, commercial, or not-for-profit sectors.

References

Airy, George B., 1856. Account of pendulum experiments undertaken in the Harton colliery, for the purpose of determining the mean density of the earth. Phil. Trans. Roy. Soc. Lond. 146, 297–355. https://www.jstor.org/stable/108589.

Barry, James P., Hashimoto, Jun, 2009. Revisiting the Challenger Deep using the ROV Kaiko. Mar. Technol. Soc. J. 43 (5), 77–78. https://doi.org/10.4031/MTSJ.43.5.27.

Beaudoin, Jonathan, Calder, Brian R., Hiebert, J., Imahori, Gretchen, 2009. Estimation of sounding uncertainty from measurements of water mass variability. Int. Hydrogr. Rev. 481, 20–38. https://scholars.unh.edu/ccom/481.

Bialek, Eugene, U.S. Naval Oceanagraphic Office, 1966. Errors in the determination of depth by pressure guages utilizing a linear pressure-depth relationship. Int. Hydrogr. Rev. 43 (1), 69–74.

Bongiovanni, Cassandra, Stewart, Heather A., Jamieson, Alan J., 2021. High-resolution multibeam sonar bathymetry of the deepest place in each ocean. Geosci. Data J. (September 2020), 1–16. https://doi.org/10.1002/gdj3.122, 00.

Carruthers, J.N., Lawford, A.L., 1952. The deepest oceanic sounding. Nature 4302, 601–603.

Chadwick, William W., Scott, L. Nooner, Mark, A. Zumberge, Robert, W. Embley, Fox, Christopher G., 2006. Vertical deformation monitoring at Axial Seamount since its 1998 eruption using deep-sea pressure sensors. J. Volcanol. Geoth. Res. 150 (1–3), 313–327. https://doi.org/10.1016/j.jvolgeores.2005.07.006.

Dahlen, F.A., 1982. Variation of gravity with depth in the earth. Phys. Rev. D 25 (6), 1735–1736. https://doi.org/10.1103/PhysRevD.25.1735.

Del Grosso, V.A., 1974. New equation for the speed of sound in natural waters (with comparisons to other equations). J. Acoust. Soc. Am. 56 (4), 1084–1091. https://doi.org/10.1121/1.1903388.

Dziak, R.P., Haxel, J.H., Matsumoto, H., Lau, S., Heimlich, S., Nieukirk, S., Mellinger, D. K., et al., 2017. Ambient sound at Challenger Deep, Mariana Trench. Oceanography 30 (2), 186–197. https://doi.org/10.5670/oceanog.2017.240.

Eble, M.C., Gonzalez, F.I., 1991. Deep-ocean bottom pressure measurements in the northeast Pacific. J. Atmos. Ocean. Technol. https://doi.org/10.1175/1520-0426(1991)008<0221:dobpmi>2.0.co, 2.

Fisher, Robert L., 2009. Meanwhile, back on the surface: further notes on the sounding of trenches. Mar. Technol. Soc. J. 43, 16–19. https://doi.org/10.4031/MTSJ.43.5.7.

Fisher, Robert L., 1953. On the sounding of trenches. Deep-Sea Res. 2 (1), 48–50.

Fletcher, Barbara, Bowen, Andrew, Yoerger, Dana R., Whitcomb, Louis L., 2009. Journey to the Challenger Deep: 50 Years later with the Nereus hybrid remotely operated vehicle. Mar. Technol. Soc. J. 43 (5), 65–76. https://doi.org/10.4031/MTSJ.43.5.26.

Foffonof, N.P., Millard, R.C., 1983. Unesco Technical Papers in Marine Science 44, Algorithms for Computation of Fundamental Properties of Seawater.

Fujimoto, Hiromi, Mochizuki, Masashi, Mitsuzawa, Kyohiko, Tamaki, Takayuki, Sato, Tadahiro, 2003. Ocean bottom pressure variations in the southeastern Pacific following the 1997-98 El Niño event. Geophys. Res. Lett. 30 (9), 1995–1998. https://doi.org/10.1029/2002GL016677.

Gallo, Natalya D., Cameron, James, Hardy, Kevin, Fryer, Patricia, Bartlett Douglas, H., Levin Lisa, A., 2015. Submersible- and lander-observed community patterns in the Mariana and New Britain trenches: influence of productivity and depth on epibenthic and scavenging communities. Deep-Sea Res. Part I Oceanogr. Res. Pap. 99, 119–133. https://doi.org/10.1016/j.dsr.2014.12.012.

Gardner, James V., Armstrong, Andrew A., Calder, Brian R., Beaudoin, Jonathan, 2014. So, how deep is the Mariana Trench? Mar. Geodes. 37 (1), 1–13. https://doi.org/10.1080/01490419.2013.837849.

Hackney, R.I., Featherstone, W.E., 2003. Geodetic versus geophysical perspectives of the 'gravity anomaly'. Geophys. J. Int. 154 (1), 35–43. https://doi.org/10.1046/j.1365-246X.2003.01941.x.

Harris, C.R., Millman, K.J., van der Walt, S.J., 2020. Array programming with NumPy. Nature 585, 357–362. https://doi.org/10.1038/s41586-020-2649-2.

Hirt, Christian, Claessens, Sten, Fecher, Thomas, Kuhn, Michael, Roland, Pail, Rexer, Moritz, 2013. New ultrahigh-resolution picture of earth's gravity field. Geophys. Res. Lett. 40 (16), 4279–4283. https://doi.org/10.1002/grl.50838.

Hunter, J.D., 2007. Matplotlib: a 2D graphics environment. Comput. Sci. Eng. 9 (3), 90–95.
IOC, SCOR, IAPSCO, 2010. Manuals and Guides, vol. 56. Intergovernmental Oceanographic Commission. The International Thermodynamic Equation of Seawater - 2010: Calculation and Use of Thermodynamic Properties.
Jalving, Bjørn, 1999. Depth accuracy in seabed mapping with underwater vehicles. In: Oceans '99 MTS/IEEE. Seattle, WA. http://ieeexplore.ieee.org/abstract/document/805004/.
Karl, John H., 1971. The Bouguer correction for the spherical earth. Geophysics 36 (4), 761–762.
Loranger, Scott, Barclay, David, Buckingham, Michael, 2021. Implosion in the Challenger Deep: echo sounding with the shock wave. Oceanography 34 (2). https://doi.org/10.5670/oceanog.2021.201.
Mathers, E.L., Woodworth, P.L., 2004. A study of departures from the inverse-barometer response of sea level to air-pressure forcing at a period of 5 days. Q. J. R. Meteorol. Soc. 130, 725–738. https://doi.org/10.1256/qj.03.46.
McDougal, T., 2010. Deriving the vertical variation of the gravitational acceleration in the ocean. http://www.teos-10.org/pubs/gsw/pdf/grav.pdf.
McDougal, T.J., Barker, P.M., 2011. Getting Started with TEOS-10 and the Gibbs Seawater (GSW) Oceanographic Toolbox, ISBN 978-0-646-55621-5, p. 28. SCOR/IAPSO WG127. http://www.teos-10.org/pubs/Getting_Started.pdf.
Millero, Frank, J., Chen, Chen-tung, Bradshaw, Alvin, Karl Schleicher, 1980. A new high pressure equation of state for seawater. Deep Sea Res. 27 (1), 255–264.
Moritz, H., 1980. Geodetic reference system 1980. Bull. Geod. 54 (3), 395–405. https://doi.org/10.1007/BF02521480.
Nakanishi, Masao, Hashimoto, Jun, 2011. A precise bathymetric map of the world's deepest seafloor, Challenger Deep in the Mariana Trench. Mar. Geophys. Res. 32 (4), 455–463. https://doi.org/10.1007/s11001-011-9134-0.
Newton, Isaac, 1687. Philosophiae Naturalis Principia Mathematica. London.
Parker, Bruce B., 2007. NOAA Special Publication NOS CO-OPS 3: Tidal Analysis and Prediction. Silver Spring, MD. https://tidesandcurrents.noaa.gov/publications/Tidal_Analysis_and_Predictions.pdf.
Piccard, Jacques, Dietz, Robert S., 1961. Seven Miles Down: the Story of the Bathyscaph Trieste. G.P. Putnam's Sons, New York, NY.
Polster, André, Fabian, Marcus, Villinger, Heinrich, 2009. Effective resolution and drift of paroscientific pressure sensors derived from long-term seafloor measurements. G-cubed 10 (8), 1–19. https://doi.org/10.1029/2009GC002532.
Puig, Jose M., 2018. Errors in pressure to depth approximations and how to avoid them. Underw. Technol. 35 (1), 3–12. https://doi.org/10.3723/ut.35.003.
Sandwell, David T., Dietmar Müller, R., Smith, Walter H.F., Garcia, Emmanuel, Francis, Richard, 2014. New global marine gravity model from CryoSat-2 and Jason-1 reveals buried tectonic structure. Science 346 (6205), 65–67. https://doi.org/10.1126/science.1258213.
Sasagawa, G., Cook, M.J., Zumberge, M.A., 2016. Drift-corrected seafloor pressure observations of vertical deformation at Axial Seamount 2013–2014. Earth Space Sci. 3, 381–385. https://doi.org/10.1002/2016EA000190.Received.
Saunders, P.M., Fofonoff, N.P., 1976. Conversion of pressure to depth in the ocean. Deep-Sea Res. 23, 109–111.
Sebera, Josef, Martin, Pitoňák, Hamáčková, Eliška, Novák, Pavel, 2015. Comparative study of the spherical downward continuation. Surv. Geophys. 36 (2), 253–267. https://doi.org/10.1007/s10712-014-9312-0.
Stewart, Heather A., Jamieson, Alan J., 2019. The five deeps: the location and depth of the deepest place in each of the world's oceans. Earth Sci. Rev. 197 https://doi.org/10.1016/j.earscirev.2019.102896. July 2018.
Taira, Keisuke, Yanagimoto, Daigo, Kitagawa, Shoji, 2005. Deep CTD casts in the Challenger Deep, Mariana Trench. J. Oceanogr. 61 (3), 447–454. https://doi.org/10.1007/s10872-005-0053-z.
Takagawa, Shinichi, Aoki, Taro, Kawana, Ikuo, 1997. Diving to the Mariana Trench by 'Kaiko'. Recent Adv. Mar. Sci. Technol. 96, 89–96.
Umbach, Melvin, J., 1976. Hydrographic Manual Fourth Edition. U.S. Department of Commerce, National Oceanic and Atmospheric Administration, National Ocean Survey, Rockville, MD.
van Haren, Hans, Berndt, Christian, Klaucke, Ingo, 2017. Ocean mixing in deep-sea trenches: new insights from the Challenger Deep, Mariana Trench. Deep-Sea Res. Part I 129 (September), 1–9. https://doi.org/10.1016/j.dsr.2017.09.003.
van Haren, Hans, Uchida, Hiroshi, Yanagimoto, Daigo, 2021. Further correcting pressure effects on SBE911 CTD-conductivity data from hadal depths. J. Oceanogr. 77 (1), 137–144. https://doi.org/10.1007/s10872-020-00565-3.
Vinogradova, Nadya T., Ponte, Rui M., Stammer, Detlef, 2007. Relation between sea level and bottom pressure and the vertical dependence of oceanic variability. Geophys. Res. Lett. 34 (3), 1–5. https://doi.org/10.1029/2006GL028588.
Virtanen, Pauli, Gommers, Ralf, Oliphant, Travis E., Haberland, Matt, Reddy, Tyler, Cournapeau, David, Burovski, Evgeni, et al., 2020. Author correction: SciPy 1.0: fundamental algorithms for scientific computing in Python. Nat. Methods 17 (3). https://doi.org/10.1038/s41592-020-0772-5, 352–352.
Williams, Joanne, Hughes, Chris W., Tamisiea, Mark E., 2015. Detecting trends in bottom pressure measured using a tall mooring and altimetry. J. Geophys. Res.: Oceans 120, 5216–5232. https://doi.org/10.1002/2015JC010955.
Willumsen, Are B., Ove Kent, Hagen, Per Norvald, Boge, 2007. Filtering depth measurements in underwater vehicles for improved seabed imaging. In: OCEANS 2007 - Europe, pp. 1–6. https://doi.org/10.1109/oceanse.2007.4302249.
Wunsch, Carl, Stammer, Detlef, 1997. Atmospheric loading and the oceanic 'inverted barometer' effect. Rev. Geophys. 35 (1), 79–107. https://doi.org/10.1029/96RG03037.
Yoshida, Hiroshi, Ishibashi, Shojiro, Watanabe, Yoshitaka, Inoue, Tomoya, Tahara, Junnichiro, Takao, Sawa, Osawa, Hiroyuki, 2009. The ABISMO mud and water sampling ROV for surveys at 11,000 m depth. Mar. Technol. Soc. J. 43 (5), 87–96. https://doi.org/10.4031/MTSJ.43.5.31.